GROWTH OF Cu_2ZnSnS_4 ABSORBER LAYER ON FLEXIBLE METALLIC SUBSTRATES FOR THIN FILM SOLAR CELL APPLICATIONS

A Thesis Submitted to
the Graduate School of Engineering and Sciences of
İzmir Institute of Technology
in Partial Fulfillment of the Requirements for the Degree of

MASTER OF SCIENCE

in Department of Physics

by
Şebnem Yazıcı

July 2014
İZMİR

We approve the thesis of **Şebnem YAZICI**

Examining Committee Members:

_____

Assoc. Prof. Dr. Gülnur AYGÜN ÖZYÜZER
Department of Physics, İzmir Institute of Technology

_____

Assoc. Prof. Dr. Alp Osman KODOLBAŞ
TUBITAK-UME

_____

Assist. Prof. Dr. Sevgi KILIÇ ÖZDEMİR
Department of Chemical Engineering, İzmir Institute of Technology

14 July 2014

_____

Assoc. Prof. Dr. Gülnur AYGÜN ÖZYÜZER
Supervisor, Department of Physics,
İzmir Institute of Technology

_____

Prof. Dr. Nejat BULUT
Head of the Department of Physics

_____

Prof. Dr. R. Tuğrul SENGER
Dean of the Graduate School of
Engineering and Sciences

ACKNOWLEDGEMENT

Foremost, I would like to express my sincere gratitude to my advisor, Assoc. Prof. Gülnur AYGÜN for introducing me to the diverse and dynamic field of photovoltaics. Experimenting with this material calls for multidisciplinary approach, combining chemistry, physics and material science. I am grateful for her, support, motivation and encouragement during my thesis.

Besides my advisor, I would like to thank the rest of my thesis committee: Assoc. Prof. Dr. Alp Osman KODOLBAŞ and Assist. Prof. Dr. Sevgi KILIÇ ÖZDEMİR, for their encouragement and insightful comments.

My sincere thanks also goes to Prof. Dr. Lütfi Özyüzer for his advices, knowledge and many insightful discussions.

I am especially grateful to my laboratory colleagues, Fatime Gülşah AKÇA, Metin KURT, Fulya TÜRKOĞLU, Hasan KÖSEOĞLU, Adnan TAŞDEMİR, Mutlu Devran YAMAN, Yasemin DEMİRHAN for their support and assistance to my work.

I would also like to thank Mehmet Ali OLGAR for his collaboration during this study.

Lastly, I offer sincere thanks to my family for their love, and unlimited patience throughout my education.

This research was supported by The Scientific and Technological Research Council of Turkey (TUBITAK) and University's Research Foundation (BAP) with the project numbers of 112T068 and 2012-IYTE-22, respectively.

ABSTRACT

GROWTH OF Cu_2ZnSnS_4 ABSORBER LAYER ON FLEXIBLE METALLIC SUBSTRATES FOR THIN FILM SOLAR CELL APPLICATIONS

This thesis presents the results of the fabrication and investigation of Cu_2ZnSnS_4 (CZTS) p-type semiconducting compound on rigid and flexible substrates, such as soda lime glass, ceramics and metallic foil substrates. The CZTS material was obtained by using a two-stage method. In the first stage, the metallic precursor was deposited by using DC magnetron sputtering technique then, the sulfurization process followed it. The particular emphasis has been placed on the distinctive substrate behavior in the growth procedure, including the microstructural characterization of the CZTS structure and the investigations of the back contact/CZTS interface. Additionally, the effect of the high temperature sulfur treatment on the formation mechanism of CZTS structure investigated elaborately. Moreover, electrical properties including the temperature dependent electrical conductivity, carrier concentrations and mobility extracted from Hall Effect measurements, and optical properties including absorption coefficient, spectral transmission, and optical band gap have been determined to characterize CZTS thin films.

Raman spectroscopy and XPS analysis of the sulfurized thin films revealed that, except for the presence of Sn-based secondary phases, nearly pure CZTS thin films were obtained. Additionally, the intense and sharp XRD diffraction peak from the (112) plane provided evidence of good crystallinity. EDS analysis indicated sufficient sulfur content but poor Zn atomic weight percentage in the films. Absorption and band-gap energy analysis were carried out to confirm the suitability of CZTS thin films for the usage as the absorber layer in solar cell applications. Finally, Hall Effect measurements showed the p-type semiconductor behavior of the CZTS samples. We aimed to investigate the role of the flexible titanium and molybdenum foil substrates in the growth mechanism of CZTS thin films. The crack formation in the CZTS layer on the Mo foils were detected, which is an indication of the incompatible thermal expansion coefficient of Mo with the CZTS structure.

ÖZET

İNCE FİLM GÜNEŞ PİLİ UYGULAMALARI İÇİN Cu_2ZnSnS_4 SOĞURUCU KATMANININ ESNEK METALİK ALTTAŞLAR ÜZERİNDE BÜYÜTÜLMESİ

Bu tez çalışmasında, p-tipi yarıiletken özelliğindeki Cu_2ZnSnS_4 (CZTS) yarıiletken bileşiğin, rijit özellikteki seramik ve cam alttaşlar ile esneyebilir özellikteki metal folyo alttaşlar üzerinde büyütülmesi ve elde edilen bileşiğin analizi amaçlanmıştır. CZTS yapısı iki aşamalı bir yöntem kullanılarak elde edilmiştir. İlk aşamada metalik öncül yapı DC mıknatıssal saçtırma yöntemi kullanılarak bahsedilen alttaşlar üzerinde büyütülmüştür. Saçtırma işlemini ikinci aşama olarak sülfürleme işlemi takip etmiştir. Bu çalışmada farklı alttaş kullanımın CZTS oluşumu üzerine olacak mümkün etkilerinin ve arka kontak / CZTS ara yüzeyinin mikro yapısal olarak incelenmiştir. Ayrıca, yüksek sıcaklıkta gerçekleştirilen sülfürleme işleminin CZTS oluşumundaki etkisi ayrıntılı olarak çalışılmıştır. Bunu dışında p-tipi yarı iletken CZTS yapının elektriksel özelliklerini belirleyen taşıyıcı yoğunluğu, mobilite ve sıcaklığa bağlı elektriksel iletkenliği Hall etkisi ve dört-nokta yöntemleriyle ölçülmüştür. Soğurma katsayısı, optiksel geçirgenlik ve optik bant aralığı gibi özellikleri de incelenerek CZTS yapısının karekterizasyonu yapılmıştır.

Raman ve XPS analizleri sülfürleme sonucu elde edilen yapıların Sn içeren ikincil fazlar dışında, tekil yapılı ince film CZTS filmlerin eldesinin başarılı olarak gerçekleştirildiğini göstermiştir. Ayrıca, öncelikli (112) kristal yönelimin oldukça yüksek bir şiddette ve keskin bir pik olarak elde edilmesi elde edilen CZTS yapısının güzel bir kristallenmeye sahip olduğu belirlendi. EDS analizi sonuçları örneklerin istenen ölçüde sülfür içerdiğini fakat Zn elementinin atomik oranın düşük olduğu görüldü. Soğurma katsayısı ve bant aralığı ölçümleri sonucu elde edilen CZTS yapısının güneş hücrelerinde soğurucu katman olarak kullanılmak üzere uygun özelliklerde olduğunu kanıtlamıştır. Son olarak Hall etkisi ölçümleri ile elde edilen CZTS yapılarının p-tipi yarıiletken özellik gösterdiği belirlenmiştir. Esneyebilir titanyum ve molibdenyum folyo alttaşların CZTS büyütmesi sırasındaki etkilerinin incelemesinin amaçlandığı bu çalışmada, CZTS yapısı ile termal genleşme katsayısı bakımından uyumsuzluk gösteren molibdenyum folyonun, CZTS yapının üzerinde yarık oluşumuna neden olduğu görülmüştür.

TABLE OF CONTENTS

LIST OF FIGURES

Figure **Page**

LIST OF TABLES

Table **Page**

CHAPTER 1

INTRODUCTION

As the World's population is continually increasing, the need for the energy also increases. Throughout the world, rapidly increasing energy demand makes the usage of oil and fossil fuels, which are limited available energy resources, inevitable. To manage to meet the worldwide growing energy demand in green and cost competitive way the utilization of clean energy sources should be promoted. This promotion could be only achieved if renewable energy sources become more accessible. That means cheaper and handy clean energy systems are needed. Solar power is the most economic, convenient and powerful energy among the other renewable energy sources. Due to its capacity to be scaled up to supply terawatts of electricity consumed by the world, the solar energy is of particular interest. The Earth receives inexhaustible and continually energy from the sun. By converting that incredible energy into the electricity cheaply and efficiently, solar energy systems become more prevalent to use as energy sources. In order to make solar energy utilization widely distributed, photovoltaic (PV) technology needs to be cost competitive with current sources of electricity.

There are several approaches to reduce the manufacturing costs of PV panels. Crystalline silicon (c-Si) is the most commonly used semiconductor for PV technology. Even though relatively high efficiency is obtained, using c-Si as light absorber material, Si solar modules requires high budget for manufacturing. However, its high cost production leads manufacturers to decrease the purity of Si and obtain less efficient but lower cost Si solar cells. The high production cost of c-Si, lead PV industry to search for cheaper candidate material as absorber layer and lower cost manufacturing.

The most efficient solar cells reaching a record of 43.5% conversion efficiency under concentrated light was achieved with multijunction solar cells connected with each other electrically in series (Wiemer et al. 2011). The epitaxy process and usage of high cost materials make multijunction solar cells considerably higher in manufacturing than other cells. Because of its high cost this type of solar cells mostly use in satellite and space applications.

By taking account the advantages of thin film solar cells like low-cost, portability, easy installation, wide range of application and high conversion efficiency, they are estimated to have potential to replace fossil fuels to meet the energy demands all around the world.

The study of solid material thin films has an old history in various application areas. In the recent years, thin film technology has developed around the world into a major research area and this subject is a major component of works in today's solid-state physics. Because of the variety of applications they offer, interest in thin films arises. Thin film physics deals with the films with thicknesses varying at a few microns, and properties of systems classified in intermediate-size, which are evaluated between atoms/molecules, and bulk materials, where phenomena length scales becomes comparable to the size of the structure. The developments in microelectronics and nanotechnology directly related to the improvements in thin film science. In present, the increase in demand for thin film materials and devices are the main reason for the development of new processes, materials and technologies with creating new opportunities to manufacture lower cost but high efficient and applicable devices. Thin films technology enables the minimization of dimensions and weight of electronic systems in very large-scale integrated circuits, for electronic packaging, sensors, transistors and devices; optical films and devices for the use of protective and decorative coatings, filters and photovoltaic device. One of the major research areas on thin film technology is applications on the photovoltaic device. Since the thin film technology provides fewer material use, and simpler processing steps as compared to a traditional wafer based crystalline solar cells, over the last few decades the thin film technology competes with Si wafer technology to take market share in PV industry. The chalcopyrite semiconductors, which are found for many compounds of composition I-III-IV, or II-IV-V, have great attraction because they have direct band gap, and high absorption coefficients and because of this, they are popular in optoelectronic applications as solar energy converters. (Weaire 1975). Chalcopyrite is a type of semiconductor.

Currently, two chalcopyrite semiconductor compounds are conventionally in used in thin film solar cell industry as an absorber layer material other than amorphous silicon (a-Si:H). They are namely, CdTe and $CuIn_xGa_{1-x}S(Se)_2$ (CIGS). Polycrystalline solar cells with a Cu(In, Ga)Se2 absorber reached recently up to 20.8 % (Jackson et al. 2014). Despite the higher conversion efficiencies of these compound semiconductors, their constituent elements cause some disadvantages in their utilizations Apart from these, Cu_2ZnSnS_4 (CZTS), (I-II-IV-VI group semiconductor compound), is a relatively

newly explored material which has a great deal of potential for use in PV energy systems. CZTS considered to be substitute for other chalcogenide-based solar cells; CIGS and CdTe. In fact, this replacement is urgently needed in the PV industry, due to the restrictions on heavy metal usage for Cd element and limited source and high cost of In and Ga elements, restrict the production capacity of these thin film solar cells. To get ideal situation in thin film PV industry, the semiconductor material in used should have two characteristics; high band-gap energy to have high absorption of incident light and, secondly, to contain non-toxic, abundant and cheap elements. Therefore, CZTS is a preferable newly explored material, which is a p-type quaternary semiconducting compound. CZTS has band gap energy around 1.4-1.5 eV, and has large absorption coefficient ($\geq 10^4$ cm^{-1}) (Katagiri et al. 1997). Beyond these beneficial physical properties, CZTS consists of earth-abundant, cheap, and non-toxic elements. These features have led researchers to focus on the CZTS compound for use in solar cell technology.

Currently, efficiencies up to 9.2% and 12.6% have been achieved for the kesterite structures Cu_2ZnSnS_4 (Hiroi et al. 2013) and $Cu_2ZnSn(S,Se)_4$ (Wang et al. 2013) , respectively. Although this is lower than the current efficiencies of other technologies, it offers less expensive and nonhazardous material usage that is crucially important for large-scale production solar cells. Theoretical calculations based on the Shockley-Queisser limit for a single p-n junction with a band gap of 1.4 eV claim that an approximately 33.7% maximum solar conversion efficiency can be generated (using an AM 1.5 solar spectrum) (Shockley and Queisser 1961). Means, more effort needs to be done to achieve higher efficiency with CZTS material. For these reasons, the CZTS compound semiconductor will be the preferred material for thin-film PVs in the immediate future.

Several methods have been used in the fabrication of CZTS thin film absorber layers, such as atom beam sputtering (Ito and Nakazawa 1988), e-beam evaporation (Araki et al. 2008), thermal evaporation (Friedlmeier et al. 1997), co-evaporation (Tanaka et al. 2006), (Schubert et al. 2011), (Katagiri et al. 2009) magnetron-sputtering (Jimbo et al. 2007) (Ericson et al. 2012) (Liu et al. 2010) (Fernandes, Salomé, and Cunha 2011), electrodeposition (Scragg, Dale, and Peter 2008), (Ennaoui et al. 2009) , spray pyrolysis deposition (Tanaka, Kato, and Uchiki 2014) (Yoo and Kim 2011), pulsed laser deposition (Moholkar et al. 2011), etc. Since thin films are so thin, they are also very fragile and they have to be formed on and are supported by a substrate. Most of

these techniques were carried out using rigid substrates such as bilayer molybdenum (Mo)-coated soda lime glass (SLG). Bilayer Mo back contact is commonly used in CIGS and CZTS solar cells due to its low resistivity and good adhesion to SLG. Mo back contact deposition requires bilayer coating owing to the fact that the bottom layer was formed at the higher working pressure to achieve a better adhesion and the top layer was deposited at the lower working pressure to get a lower resistivity. However, the deposition of the thin film absorber layer on flexible substrates may open many new application areas for large area thin film solar cell fabrication (Winkler et al. 2004) .

Metallic foils, such as Cr-steels, titanium, molybdenum, aluminium and some alloys are promising flexible substrates because they are cheap, lightweight, durable, and resistant to high-temperature fabrication processes. The preferential flexible substrates should have well-matched coefficients of thermal expansion (CTE) (i.e.,5–12x10^{-6} K^{-1}), sufficient thermal (T ≥400°C) and chemical resistivity (especially against S and Se), and should be suitable for roll-to-roll deposition, in addition to being cost efficient (Kessler and Rudmann 2004). Additionally, metallic flexible substrate utilization eliminates the need for the deposition of a metallic conductive back contact layer. As a result, the cost of manufacturing and constructing solar cell modules would be substantially lowered. Therefore, it becomes one of the vital areas of the thin film works. The crystallographic form of films and many of their properties depend on substrate conditions.

Growth of CZTS layer on the flexible Mo foil has only been investigated via the solvothermal approach (Dai et al. 2012a). Deposition of CZTS layers on flexible polyimide substrates were carried out using a screen printing process(Zhou et al. 2010a) and electrochemical deposition technique (Farinella et al. 2014). To the best of our knowledge, investigations of CZTS absorber layer growth on metallic flexible substrates via magnetron sputtering followed by sulfurization have not yet been conducted.

In the present work, magnetron-sputtering technique was used in the first stage of the growth mechanism since sputtering offers a wide range of advantages, such as easy adaptation to large-scale and reproducible manufacturing. Additionally, we chose to study with both Ti and Mo foils substrate, due to the preferable CTE and chemical inertness behavior of Ti element, and Mo foil was used to compare the results with Ti foil.

CHAPTER 2

THE PHYSICS OF PHOTOVOLTAICS

Similar to other fields of technology, the first step to achieve success in solar energy utilization is to have necessary scientific background knowledge. The essential concept in solar cells is the p-n junction. Therefore, an adequate understanding of the semiconductor physics is inevitable.

Solar cells are made of semiconductor materials. A semiconductor is characterized by its bandgap energy value (eV). In a semiconductor material, valance band electrons can be excited to the conduction band by a photon, consequently an electron-hole pair is formed. After formation of electron-hole pairs, the electric field of p-n junction separates electrons and holes to generate free carriers, thereby the external electric current. Before giving the details of this physical phenomenon, an elaborate explanation of semiconductor physics is necessary.

2.1. Characterization of Semiconductors

The name ‘semiconductor’ originate from the fact that such materials have conductivity higher than that of the insulators, and lower than that of the conductors. That is not the only specialty with such material’s conductivity. In particular, semiconductor’s conductivity depends on very strongly on material state, such as, chemical purity and temperature, much more than in the case for metals. For pure semiconductors, the conductivity decreases while cooling down from room temperature to liquid helium temperature. At absolute zero temperature, conductivity almost vanishes, in opposite to metals, which increases as temperature decays. The conductivity of metals reaches its maximum at low temperature. Considering the semiconductor conductivity dependence on purity, a very pure semiconducting material behaves as an insulator, while a high degree impurity state leads to metal like behavior in semiconductors. Moreover, interaction with light can lead to a transition from insulator-like behavior to metal-like behavior of a semiconductor material. The other optical properties shared by semiconductors: the threshold frequency of incident light to be absorbed in a semiconductor material-

below the threshold frequency, light just transmits, while the light with the above this frequency is strongly absorbed within the semiconductor material. Furthermore, luminescence properties in the visible and infrared range are also characteristic property for these materials. All these unique features of semiconductors can be well explained by the band theory.

2.2. Electrons in an Atom

An electron in an atom sees Coulomb interaction with the nucleus and other electrons in the atom. For an electron, only certain electronic energy levels are allowed to be placed. These levels can be examine in two distinct regions.

Free states: An electron in these states is not confined near the atom. The attractive potential of the atom cannot overcome electron's high kinetic energy in these states. Al energies are allowed in these states (Figure 2.1.).

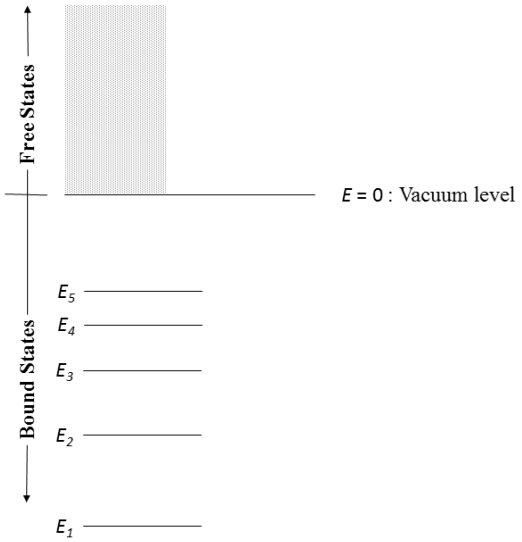

Figure 2.1. A schematic of electron energies in an atom

Bound states: Opposite to the free states, the all energy levels are not allowed in bound states, where the electron wavefunction is confined to ~1Å around the nucleus. Only certain discerete energy levels are allowed for electron to be present as shown in Fig. 2.1. The bound and free states form the allowed energies. The allowed energies in the bound states separated by forbidden energy gaps.

The vacuum level is the energy at which the electron becomes free. By taking the vacuum level as a reference energy, the bound state energies are negative since the electrons are under an attractive potential. The lowest energy state is called the ground state (n=1).

$$E_n = \frac{-m_0 e^4}{2(4\pi\varepsilon_0)^2 \hbar^2 n^2} \tag{2.1}$$

2.3. Electrons in Crystalline Solids: Energy Bands

If the neighboring atoms are more than a few angstroms away from each other, atoms will not influence by the adjacent atoms. The energy states will look just as they would in an isolated atom. This is shown schematically on the left-hand side of Fig. 2.2. However, when the atomic distance is 1-2 Å, the neighboring atoms and nuclei will influence electrons. The results of these interactions can be listed:

- The lower energy states are relatively unaffected by the presence of the adjacent atoms and remain similar like they are in isolated atoms.
- The higher energy levels broaden into a "band" of allowed energy levels. Instead of just one sharp allowed energy level, bands of energies become allowed.
- These allowed bands are separated by bandgaps.

The electron, within each allowed bands, is described by a k-vector, as in free space. In free space electrons are described by these three basic equations (V_o is the uniform background potential)

$$\text{Energy: } E(k) = \frac{\hbar^2 k^2}{2m_0} + V_0$$

$$\text{Momentum: } \mathbf{p}(k) = \hbar \boldsymbol{k}$$

$$\text{Equation of Motion: } \hbar \frac{d\mathbf{k}}{dt} = \boldsymbol{F}_{ext} \tag{2.2}$$

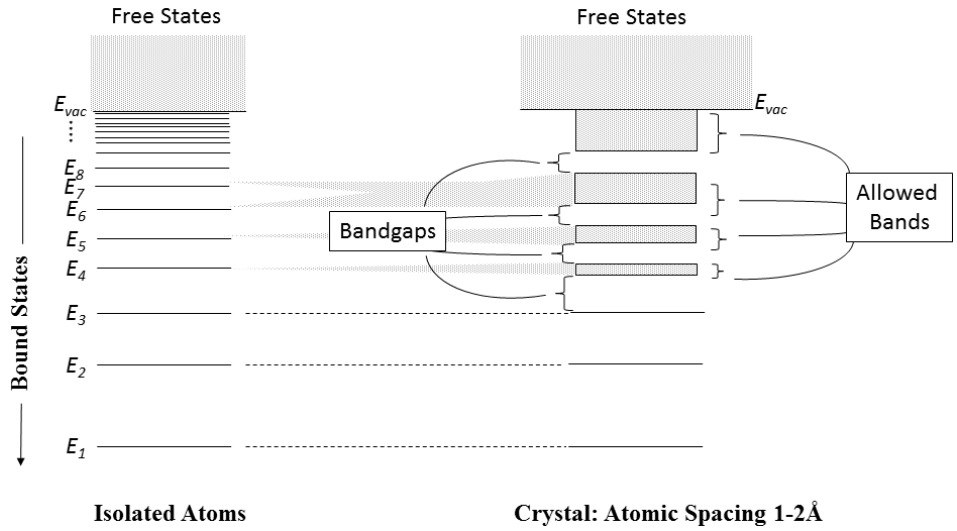

Figure 2.2. Electron energy levels in isolated atoms and in crystals

Within a crystal, in these bands, electron behaves as if it were in a free space, except it responds as if it had a different mass known as effective mass (m*). This is a one of the result of the band theory of solids. The movement of an electron in a periodic crystalline potential can be different than it is in a vacuum environment. The effective mass can be greater or smaller than the free electron mass. Due to the crystalline forces, the electron responds to these forces as if it had a new effective mass.

The equation of motion of an electron in perfect crystal, alike if it in free space is

$$\hbar \frac{d\mathbf{k}}{dt} = \boldsymbol{F}_{ext} \tag{2.3}$$

and the relation between energy and the effective momentum (ħk) is

$$E(k) = \frac{\hbar^2 k^2}{2\,m^*} + V_0 \tag{2.4}$$

Now, V_o is the launching energy of the allowed band.

These electronic states are the solutions of the Schrödinger equation. Formation of these states does not mean these electrons occupy these states. Distribution of electrons in these allowed states follows a distribution function *f* (E). This distribution function is given by the Fermi-Dirac distribution (at thermal equilibrium at temperature T). *f* (E) gives the probability that an allowed energy state E is occupied.

$$f(E) = \frac{1}{1+ e^{\frac{E - E_F}{k_B T}}} \quad (2.5)$$

This expression denotes that f (E) is always less than one, as shown in Fig. 2.3. At T=0 K, the Fermi function is step function. Here E_F is called Fermi level. As temperature increases, the function starts to develop an exponential tail. At the Fermi energy, f (E) goes to 0.5. In the case of $(E-E_F) >> k_BT$, the unity in the denominator can be ignored. In this case, the Maxwell-Boltzmann distribution, which is widely used in semiconductor device physics, is obtained (Eq. 2.6).

$$f(E) = \frac{1}{e^{\frac{E-E_F}{k_B T}}} \quad (2.6)$$

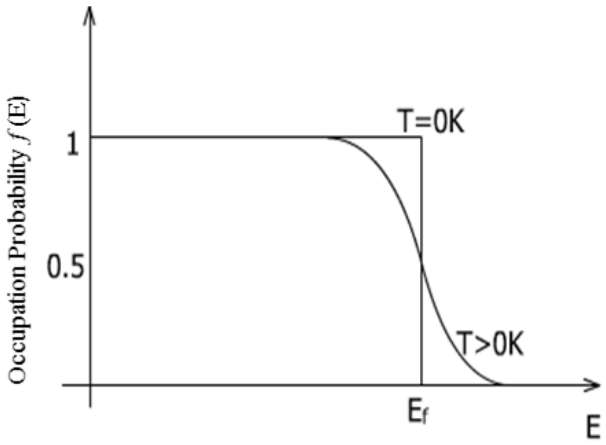

Figure 2.3. The Fermi distribution function at various temperature

2.4. Energy Band of a Semiconducting Material

All solids can be classified as conductors, semiconductors or insulators according to the availability of conduction electrons in their structures. Band Theory explains these differences in electrical characteristics of solids. A huge number of atoms comes together to form a solid. Simultaneously, the wavefunctions of electrons of these atoms interact with each other and forms extended quantum states. After all, infinite number of energy bands formed. According to the Pauli Exclusion Principle, each state can only be occupied by one electron. According to the relative position of the energy bands and the

Fermi energy level, there are three different cases (Fig.2.4). The highest occupied energy level is in the middle of an energy band.

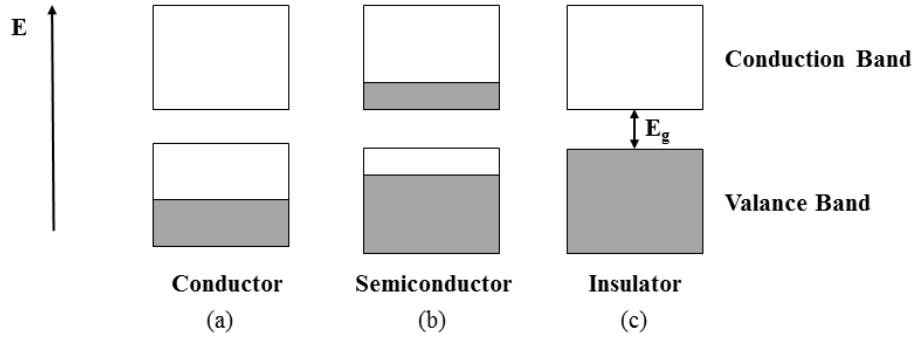

Figure 2.4. Electron occupancy of conductor, semiconductor, insulator

If an allowed band is completely filled with electrons, these electrons in the band cannot conduct any current. If this is not the case, the electrons can move to the unoccupied parts of the energy band. This type of material is called a conductor or a metal. If the highest occupied energy level matches the top of an energy band, which is called the valence band, marked as E_v, and the distance to the next energy band is large, the electrons are not easily excited to the higher band. This type of materials is called an insulator. An important case between those two is the semiconductor, where the gap between the top of the valance band E_v and the bottom of the next energy band E_c is small such that when the temperature is not too low electrons can be excited to the next anenergy band, the conduction band. The band that is normally filled with electrons at 0 K in semiconductors is called the valance band while the band above the E_g is called the conduction band. Typically, the energy gap is less than a few electron volts. Once the electrons are excited to the conduction band, some conduction can take place.

The energy difference between the vacuum level and the Fermi level is called the metal work function ($q\Phi$). The energy difference between the vacuum level and bottom of the conduction band is called the electron affinity ($q\chi$) (Figure 2.5.).

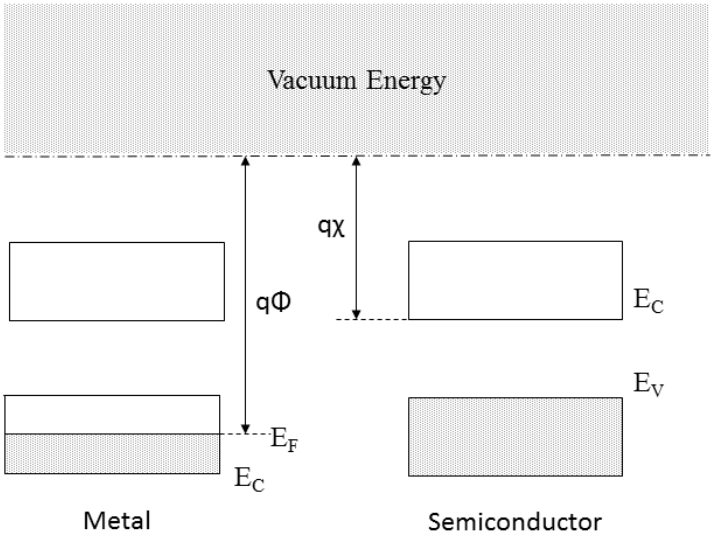

Figure 2.5. Schematically illustrated electron occupation of the bands in a metal and semiconductor

As a summary, metals have very high conductivity since very large number of electrons can participate the current transport. On the other hand, semiconductors at 0 K the highest occupied band is completely filled as a result cannot carry any current and behave as an insulator. However, as the temperature is increased, the Fermi function smears and a few empty states appear in the valance band since these electrons excited to the conduction band. Current transportation takes place at higher temperatures than absolute zero kelvin.

Every semiconducting material has its own unique band structure. Schrödinger equation solution for an electron in a semiconductor crystal give the E-k relation (energy versus effective momentum relation). In a semiconductor lattice, the E-k diagram that represents the range of energy and momentum that an electron within a crystal lattice can have describes the states of electron and hole (Figure 2.6.).

For some semiconductor materials, the bottom of the conduction band occurs at k=0. Such semiconductors such as GaAs, InP are called direct band gap semiconductors. In other group of semiconductors, the bottom of the conduction band does not occur at k=0. Such semiconductor materials like Si, Ge, AlAs are called indirect band gap semiconductors. The importance with the direct or indirect band gap materials is that, this alignment has a strong effect in the interaction of semiconductors with the light. Indirect band gap material Si has relatively poor optical properties. The elaborate explanation about E-k diagram and band gap of a semiconductor is given in Section 2.10.1.

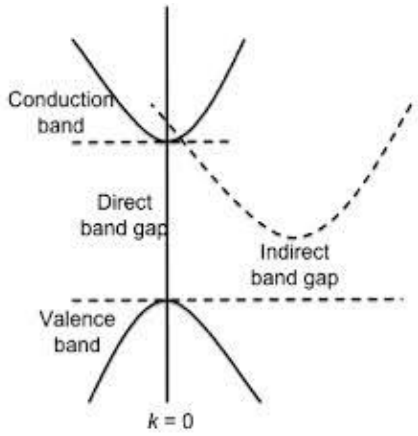

Figure 2.6. Schematically illustrated the valance band, direct band gap and indirect band gap conductions

The band structure can be simply represented by the relation (Eq. 2.7)

$$E(\boldsymbol{k}) = E_C + \frac{\hbar^2 k^2}{2m^*} \tag{2.7}$$

where E_c is the conduction bandedge. This equation denotes that the band structure is a parabola. Additionally, this equation for the E-k relation is resembles of energy of an electron in free space (Eq.2.2) except that the free electron mass m_o is replaced by m^*. Since the effective mass of material is obtained by by fitting the actual E-k diagram by a parabola, for a indirect band gap semiconductor material the effective mass concept becomes more complex. For Si and Ge, effective mass for density of states calculations should be carried out.

Direct band gap compound semiconductor materials have preferable properties. The direct band gap ensures good optical and better electron transport in the conduction band.

2.5. Semiconductor Materials

Semiconductors can be classified in two groups as elemental and compound semiconductors. Group IV elements constitutes the elemental semiconductor and the compound semiconductor materials are formed from special combinations of group III-V and group II-VI elements. Table 2.1 lists a few of the most commonly used semiconductor materials and Table 2.2 shows a portion of the periodic table.

Table 2.1. List of some semiconductor materials

Elemental Semiconductors	
Si	Silicon
Ge	Germanium
Compound Semiconductors	
AlP	Aluminium phosphide
AlAs	Aluminium arsenide
GaAs	Gallium phosphide
InP	Indium phosphide
ZnO	Zinc oxide
ZnS	Zinc sulfide
CdSe	Cadmium selenide
CdTe	Cadmium telluride

Table 2.2. A portion of the periodic table

I a	II a	III	IV	V	VI
		B	C	N	O
		Al	Si	P	S
Cu	Zn	Ga	Ge	As	Se
Ag	Cd	In	Sn	Sb	Te
Au	Hg				
.....	.....				

The elemental semiconductors referred to as group IV semiconductors compose of single species of atoms. Group IV semiconductors have diamond crystal structure. Silicon is by far the most common indirect band gap semiconductor that is used in microelectronics. Si atom has four outer electrons available for chemical bonding. The remaining ten electrons are tightly bound the nucleus. In a crystal of Si, each atom bonds to four other Si atoms, and each bonds consists of two electrons. This type of bonding, where the atoms involved share the electrons is called covalent bonding. This is an atomic bond that tends to achieve closed-valance energy shell, an example of which is found in the hydrogen molecule. A significant difference between the covalent bonding of hydrogen and group IV elements is that, when an hydrogen molecule is formed it has no additional electrons to form additional covalent bonds, while the outer silicon atoms forms additional covalent bonds with present valance electrons. This four nearest neighbours in silicon forming the covalent bonds corresponds to the tetrahedral crystal system and the diamond structure.

Mixing semiconductors to produce an alloy is also possible. The binary compound direct band gap semiconductors crystallize in zinc blende (sphalarite) and/or wurtzite structure. The zinc blende structure differs from the diamond structure since there are two different atoms in the lattice.

The ternary (three-element) or more complex quaternary (four-element) semiconductor compounds can also be formed that provide flexibility with options of using different elements. An example is $Ga_{x}In_{1-x}As$, in which the subscript indicates the fraction of the lower atomic number element component. Additionally, if A and B are two semiconductors with the lattice constant a_A and a_B, the lattice constant of an alloy $A_{x}B_{1-x}$ can be calculated by Vegards's law (Eq. 2.8).

$$a_{all} = xa_A + (1-x)a_B \tag{2.8}$$

2.6. Mobile Carriers: Intrinsic Carriers

In a semiconductor, no current flows due to the filled valance band and empty conduction band. However, if some empty states (holes) are created in the valance band, electron transportation can take place through the holes. Similarly, if the electrons are placed in the conduction band, they can curry the current. These are called mobile carriers. If the density of electron in the conduction band is n, the holes density in the valance band is p, p+n the total mobile carrier density is obtained.

Placing these mobile carriers into valance or conduction band can be carried out in two ways. In a pure semiconductor, at temperatures higher than absolute zero kelvin, the thermal energy of the crystal is enough to dislodge an electron from valance band and to excite it to the conduction band. In this way an electron-hole pair is formed. The other way to create mobile carriers is due the naturally formed crystallographic defects, which will be discussed in section 3.5: Structural Properties of Polycrystalline Thin Films.

In a pure semiconductor electron and hole density is equal to n_i and p_i, respectively. The subscript i refers to intrinsic. The intrinsic carrier concentrations namely electrons present in the valance band, and holes are in the conduction band. The intrinsic carrier concentration depends on the band gap and the temperature. *N(E)*, the density of states (DOS) gives the number of states per unit volume and energy between E and

E+dE for the conduction ($N_C(E)$) and valance band ($N_V(E)$) , respectively. For energies that are close to extrama points of these two bands, the density of states has a quadratic E dependence (Figure 2.7(a)). The concentration of electrons in the conduction band is,

$$n = \int_{E_C}^{\infty} N_e\,(E) f(E) dE \tag{2.9}$$

where $N_e(E)$ is the electron density near the conduction bandedge and $f(E)$ is the Fermi function.

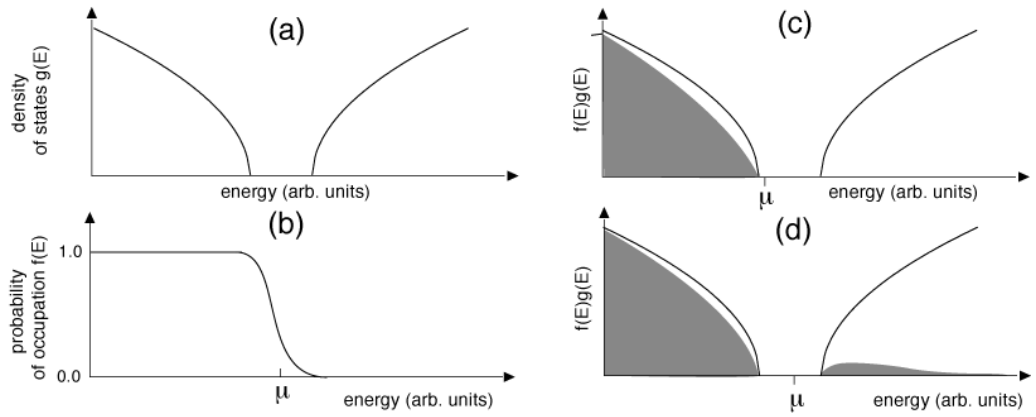

Figure 2.7. a) Schematic density of states for a semiconductor. (b) Fermi-Dirac distribution. (c) Occupied density of states (grey area) for the chemical potential just above the valence band maximum. (d) Occupied density of states for the chemical potential close to the middle of the gap. Note that the temperature in (c) and (d) is much higher than room temperature to make the presence of excited carriers visible

By using appropriate expressions, we may calculate the conduction band density of states from Eq.(2.9),

$$n = \frac{1}{2\pi^2}\left(\frac{2m_e^*}{\hbar^2}\right)^{3/2} \int_{E_C}^{\infty} \frac{(E-E_C)^{1/2}}{\exp\left(\frac{E-E_F}{k_B T}\right)+1} \tag{2.10}$$

$$= 2\left(\frac{m_e^* k_B T}{2\pi\hbar^2}\right)^{3/2} exp[(E_F - E_C)/k_B T] \tag{2.11}$$

In the case of Fermi level is far from bandedge, the unity in the denominator can be neglected. This is called Baltzmann approximation and is valid when n is small enough ($<10^{17}$ cm^{-3}). Then we obtain

$$n = N_C exp[(E_F - E_C)/k_B T] \tag{2.12}$$

where N_C is the density of states at the conduction bandedge,

$$N_C = 2\left(\frac{m_e^* k_B T}{2\pi\hbar^2}\right)^{3/2} \tag{2.13}$$

By using the same approximation (E_F-E $\gg$ k_BT) and carrying out the same mathematics, we may calculate valance band density of states.

$$p = 2\left(\frac{m_h^* k_B T}{2\pi\hbar^2}\right)^{3/2} exp[(E_V - E_F)/k_B T] \tag{2.14}$$

$$= N_V exp[(E_V - E_F)/k_B T] \tag{2.15}$$

$$N_V = 2\left(\frac{m_h^* k_B T}{2\pi\hbar^2}\right)^{3/2} \tag{2.16}$$

where N_V is the density of states for the valance bandedge.

As mentioned earlier for intrinsic semiconductors hole concentration is equal to the electron concentration. By multiplying the n and p,

$$np = 4\left(\frac{k_B T}{2\pi\hbar^2}\right)^3 \left(m_e^* m_h^*\right)^{3/2} exp\left(-E_g/k_B T\right) \tag{2.17}$$

The carrier concentration increases exponentially as the band gap decreases and it is dependent on temperature. It can be clearly seen now that the product of np is independent of the position of the Fermi level. This is called *the law of mass action.* It says when n increase, p must decrease, and vice versa (for intrinsic semiconductor $n=n_i$ and $p=p_i$).

Additionally, by setting n=p the Fermi level position can be obtained,

$$E_{Fi} = \frac{E_C + E_V}{2} + \frac{3}{4} k_B T ln\,(m_h^*/m_e^*) \quad (2.18)$$

Equation 2.18 says, the Fermi level of an intrinsic semiconductor material lies close to the midgap.

2.7. Doping: Extrinsic Carriers

By introducing special impurity atoms into a pure semiconductor electron and hole density can be altered. In this way, electron transportation can take place. Impurity atoms able to modify the electrical properties of the semiconductor material and make it suitable to use in integrated electronic circuits (diodes, transistors, light emitters, detectors, etc.). There are two different kind of dopant atoms. *Dono*r impurity atoms donate an electron to the conduction band and forms n-type semiconducting behavior. On the other hand, *acceptor* atoms accept an electron from the valance band and create a hole in this band and p-type semiconducting take place.

For elemental semiconductors (group IV) n-type impurities are P, As and Sb (group V elements) while p-type impurities are group III elements, namely B, Al, Ga and In. For group III-V compound semiconductors such as GaAs, for n-type doping group V element As should substitute with elements from group VI. This provides an extra electron in the compound ant n-type conductivity is obtained. Similarly, for p-type doping group III element Ga replaced by a group II element, which acts as an acceptor.

Focusing on pentavalent (donor) atom doping in Si, four of the outer electrons of the donor atom bonds to a Si atom, remaining fifth electron is now sees a positively charged ion to which is attracted. This attraction is simply a coulombic attraction and it is compensated with dielectric constant of the material. The lowest-energy solution for this problem is

$$E_d = E_C - \frac{e^4 m_e^*}{2(4\pi\varepsilon)^2 \hbar^2} \quad (2.19)$$

where E_d donor energy level and ε is dielectric constant. The ground state is shown schematically in Fig 2.8(a). The energy level is measured from the bandedge. Similarly,

for acceptor impurity doping the band diagram of the host semiconductor is shown in Fig. 2.8(b).

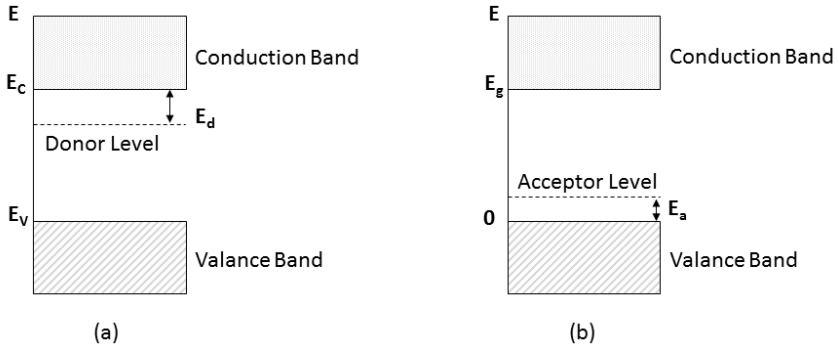

Figure 2.8. Schematically description of (a) donor level, (b) acceptor level

2.8. p-type and n-type Semiconductors

Semiconductors conductivity critically depends on the type and concentration of impurities. According to the position of the energy level of the atoms in the band gap of a semiconductor, there are two major types of impurities, donors and acceptors. Donors donate an electron to the conduction band of the semiconductor, while acceptors accept an electron from the valance band, in this manner creates a hole. Therefore, a semiconductor doped with impurities, which are ionized (since impurity atoms either have donated or accepted an electron) will therefore contain free charge carriers. Ionized donors provide an excess free electron in a semiconductor, which is then called n-type semiconductor, while an ionized acceptor provide free holes forms p-type semiconductor material.

2.9. Formation of p-n Junction

pn- junction is the corner stone of the electronic age. Most semiconductor devices contain at least one junction between p- and n-type semiconductor materials. The pn-junction provides electronic circuit functions.

Figure 2.9 is a schematic illustration of a p-n junction. When a p-type semiconductor and an n-type semiconductor are brought together, a built-in electric field is established. Initially, there is a very large density gradient in both electron and hole concentration. Because of the random thermal motion of the free electrons, they start to

diffuse from n-type region to the p-type region, and majority carriers holes in the p-type region diffuse into the n-type region. As electrons diffuse from n-type region, they leave behind positively charged donor atoms. Similarly, holes diffusion from p-region leads the formation of negatively charged acceptor atoms. These negatively and positively charged fixed ions induces an electric field, namely built-in electric field at the junction.

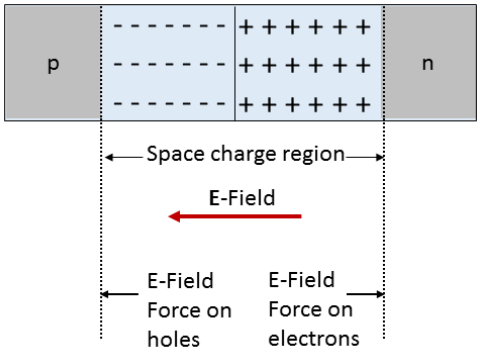

Figure 2.9. The space charge region, the built-in electric field and the force acting on the charge carries

The free charge carriers adjacent to junction are influenced by this built-in electric field; electrons being attracted towards to positive ions and holes being attracted towards negative ions. Means, a mobile electron or hole near the space charge region (or namely, depletion region) will be attracted by the built-in electric field and drift into its original volume. These two opposing flows eventually reach a stable equilibrium. Then, the net flow of electrons across the junction is zero. Even though there is no net flow of current across the junction, there has been an established electric field, this electric field is the basis of the operation of pn- junction devices.

Depletion region is an insulator region since all the mobile charges have diffused away, leaving only fixed charges associated with dopant atoms. Since this region is depleted from the mobile charges, it is named *depletion region*. The depletion region thickness can be modified by adding an external electric field (forward or reverse bias) to the built-in electric field. I can be greater by adding electric field with the same direction of built-in electric field, vice versa. This is the reason the depletion region can be considered to operate as voltage-controlled resistor.

If positive voltage is applied to the p-type region *forward bias* takes place. Since this battery induced field and built-in field are in opposite direction, the resultant field is smaller. Means, depletion region gets thinner, resistivity exponentially decreases (expo-

nential region) (Figure 2.10). If the applied voltage is large enough, the depletion region's resistance becomes negligible.

If negative voltage is applied to the p-type region *reverse bias* is formed. This time battery induced field and built-in filed are in the same direction, and the resultant field is larger. Therefore, depletion region becomes thicker and gets more resistive. As the applied reverse bias voltage becomes larger, the current flow will saturate at a constant but very small value. Because current flows only when it is forward biased, the diode works as an electrical one-way valve.

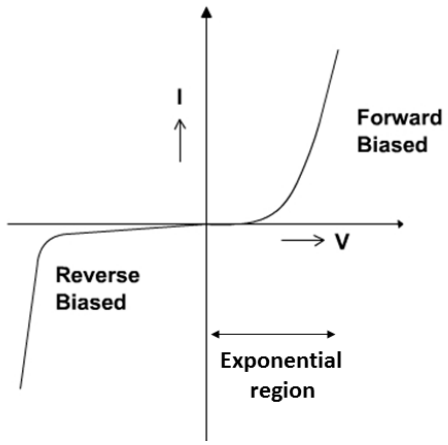

Figure 2.10. I-V characteristic of pn-junction diode

2.10. Operational Principle of Solar Cells

The solar cell is a solid-state device that converts sunlight, as a stream of photons, into electrical power. When light shines on a solar cell, it can generate current and voltage.

According to the theory of quantum transitions photons interact with a semiconductor in two ways; photon with energy greater than the gap energy of the semiconductor material can be absorbed and create an electron–hole pair. An electron–hole pair can recombine and emit a photon of energy roughly equal to the energy gap of the semiconductor. According to the principle of detailed balance, the probabilities of these two processes should equal. This fact has a significant consequence to the efficiency of solar cells.

Working principle of solar cells is based on the photovoltaic effect. The basic processes behind the photovoltaic effects are,

- Generation of free electron-hole pairs due to the absorption of light in a p-type semiconductor material which forms junction with a n-type semiconductor,
- Subsequent separation of these photo-generated electron-hole pairs in this junction,
- Collection of photo-generated free charge carriers at the back and front electrodes.

When light shines on a solar cell, it can generate current and voltage. The reason this can happen is, the built-in electric field at the junction. Because of the built-in electric field, the electrons attracted towards the p-type ions in the n-type semiconductor material side and vice versa. This separation causes a current to flow across the junction from n-type to p-type. Namely, conventional current.

For every photo-generated electron, corresponding hole is generated, simultaneously. These elecrons and holes can remain excited only for a short time since the electron-hole pairs are physically very close to each other. In a process called *recombination,* these two opposite charge carriers fall back into the bounded position. Their electrical energy is lost as heat.

Finally, by attaching a wire (load) the power along the external circuit can be obtained. This photo-generated current is opposite in direction to forward bias current. Electric current can be measured simply by a serial attached current meter. Because the resistance across the wire and current meter is low, it will be like no voltage across the solar cell, but the current flow. This situation is called *short-circuit current*. The light generated current depends on the intensity of the incident light and the recombination rate.

Power can be obtained from the solar cell as long as it produces both voltage and current. Let us consider the situation of the wire get cut, there is no pathway for photo-generated current to flow, but separation of electrons and holes keeps continue inside solar cell. Now, instead of the current flow, *a build up* voltage forms across the solar cell-positive voltage on the p-type region and negative voltage on the n-type region. This situation, where no current flow but voltage formation is called the *open-circuit voltage*. This voltage drop can be measured by adding a voltmeter across the illuminated solar cells. The build up voltage reaches a point where the forward bias current balances the photo-generated current. These two currents cancelling each other out. The voltage at this occurs is named open circuit voltage.

In order to get an output power from a solar cell there need to be right valued resistance between the contacts.

2.10.1. Absorption of Light in Semiconductor

A solar cell structure consists of an absorber layer where the photons of incident radiation are absorbed and results in creation of electron-hole pairs. If the incident light has enough energy, it can break some of the chemical bonds of the absorber semiconductor material. Means, it can excite an electron from valance band to conduction band. In semiconductor material, absorption conditions are completely based on the band gap of the material and the photon energy.

Absorption of photons in a semiconductor material relies on a complex interaction of light with the semiconductor's atomic structure. In a semiconductor lattice, the states of electron and hole are described by the energy-momentum (E-k) diagram that represents the range of energy and momentum that an electron within a crystal lattice can have. This diagram is generally drawn for the particular crystal direction in which the energy separation between the conduction band minimum and the valance band maximum, which is band gap. The physical separation between the adjacent atoms determines the minimum conduction-valance band energy. In a crystal, the interatomic distances are different along different directions means, the energy separation is directionally dependent. The E-k diagram is conventionally drawn with electron energy increasing in the upward vertical direction, while hole energy increasing in the downward vertical direction (Figure 2.11).

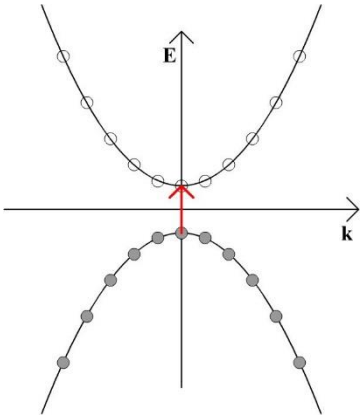

Figure 2.11. The E-k diagram for k=0

It can be seen in the E-k diagram that an electron in an energy state, there are several momentum values in that state an electron can have. The electron-hole transition that occur between the valance and conduction can either be vertical, means undergoing just a change in the energy, or diagonal, undergoing a change in both energy and momentum. In both case, energy and momentum conservations must be relevant for both charge carriers, electron and hole. Due to the selection rules, different transitions take place at different levels of conduction and valance band filling. Transitions can only take place when an electron has been removed from valance band to free-up an energy level, which the hole can move. The removal of electrons from valance band is achived temporarily by exciting the electrons, or permanently by p-doping. Therefore, these transitions determine the semiconductor material's absorption spectrum, which depends on the band's population, namely density of electrons and holes in the material.

A charge carrier within the crystal is subjected to force,

$$F = m^* \times a \tag{2.20}$$

where m* is the effective mass. Then, the kinetic energy of a charge carrier in a crystal is,

$$E = \frac{p^2}{2m^*} \tag{2.21}$$

where p is the momentum of the charge carrier

$$p = \hbar k \tag{2.22}$$

where ħ is the reduced Plank's constant (h/2π). By substituting the equation 2.21,. The equation 2.22 becomes,

$$E = \frac{\hbar^2}{2m^*}\, k^2 \tag{2.23}$$

In this simplified model the energy bands are knows as parabolic with momentum, k. During electron excitation, a photon is absorbed by an electron and its energy state changes. The energy difference between the final and initial state of the electron is equal to the energy of photon (Eq.2.24).

$$E_e - E_a = h\nu \tag{2.24}$$

where E_e is the original energy of the crystal, E_a is the final state of the crystal after the photon is absorbed. h is the Planck's constant, and ν is the frequency of the corresponding photon.

The matching equations for the energies of an electron in the conduction band and hole in the valence band are as follows which are just results of conversation of energy and momentum:

$$E_e - E_c = \frac{p^2}{2m_n^*} \tag{2.25}$$

$$E_v - E_a = \frac{p^2}{2m_p^*} \tag{2.26}$$

where E_c is the conduction band minimum, E_v is the valance band maximum, m_n^* and m_p^* are the effective masses of electrons and holes, respectively.

By adding the these two previous equations together and by using the fact that separation between the conduction band minimum and the valance band maximum is the band gap of the semiconductor material;

$$h\nu - E_g = \frac{p^2}{2}\left(\frac{1}{m_n^*} + \frac{1}{m_p^*}\right) \tag{2.27}$$

This equation hold for the direct band gap semiconductors, because absorption conditions completely based on the band gap of the material and the photon energy. According to this equation, the crystal momentum increases with energy, but as discussed before absorption must depend on the density of electrons and holes in the material. The density of electrons increases downward in energy from the valence band edge, while the density of holes increases upward in energy from the conduction band edge. Means absorption coefficient increases with increasing photon energy above E_g of the material. Using the equation 2.27, and a theoretical treatment, we obtain the expression for the absorption coefficient of a direct semiconductor .

$$\alpha(f) = C\left(h\nu - E_g\right)^{1/2} \tag{2.28}$$

α is the absorption coefficient of a semiconductor material, C is the constant which is $2x10^4$ for all direct band gap materials if α is expressed in cm^{-1} and $h\nu$ and Eg in eV.

Absorption of photons resulted in the generation of free charge carriers in a semiconductor, electrons and holes. The generation of free charge carriers is a result of breaking of the atomic bonds, when the electron-hole pairs are created.

2.11. Operational Principle of Thin Film Solar Cells

Thin film solar cell operation principle is based on the p-n heterojunction formation by placing electronically dissimilar two semiconductor materials together. The p-n heterojunction forms with the connection of a p-type semiconductor, which behaves as an absorber layer and the n-type transparent conducting oxide (TCO) material. Thin film solar cells consist of layers of different materials in thin film form.

The TCO is highly doped in order to extend the space-charge region of the p-n junction deep into the p-type absorber layer. When the electrons absorb the photons of light with energy greater than the energy band gap (E_g) of the absorber layer, the electrons in this p-type layer are excited to higher energy levels in the conduction band and leave an empty state (hole) in the valance band. These excited electrons in the conduction band move away from the holes in the valance band by the electric filed formed in the space charge region. In this manner, they maintaining a voltage for recombination through an external circuit.

Obtaining high efficiency from thin film photovoltaics relies on two issues; high conversion efficiency of incident solar photons into the charge carriers and high collection efficiency of these photo-generated free carriers in terminals. The main problem needs to be tackled in heterojunction devices is the effect of the bandgap discontinuities and different material properties.

As shown schematically in Figure 2.12, thin film solar cells consist of a substrate that holds the thin film layers on it, two electrical contact layers to carry the current (back contact and front contact), p-type absorber material where the incident photons with suitable energy are absorbed, n-type TCO (window) layer to draw the current to the outer circuit.

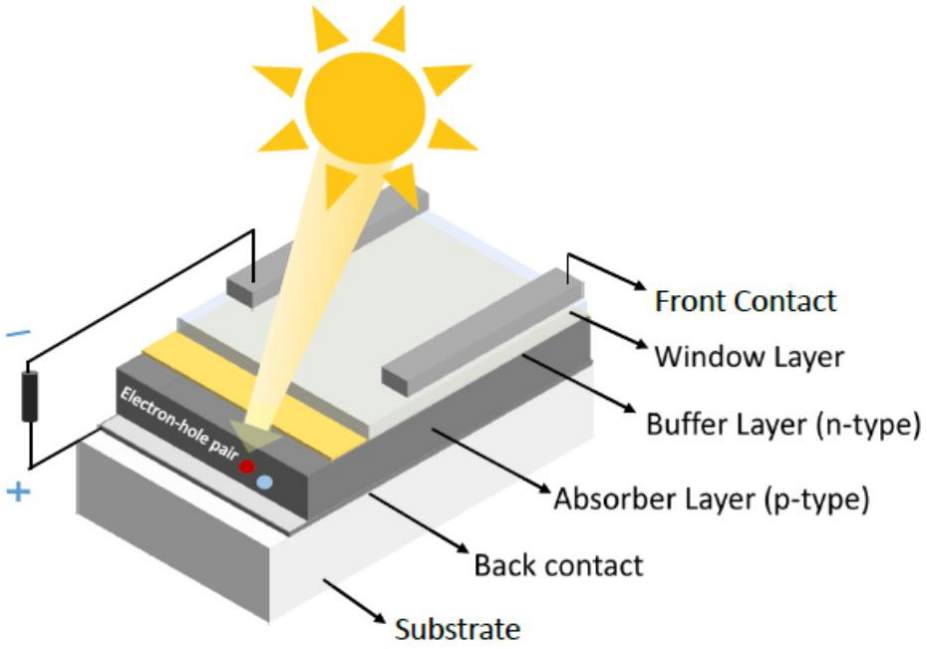

Figure 2.12 Schematic of a thin film photovoltaic device

Additionally, a buffer layer is necessary to form the junction with the absorber layer and make moderate band alignment between absorber and window layer. Each material has distinct physical and chemical properties that affect the overall performance of the thin film solar cell. Understanding the behavior of each component is essential to design high efficient devices. Furthermore, since each layer is composed of different material, each layer has different crystal structure, lattice constant, electron affinity, work function, thermal expansion coefficient (CTE), chemical affinity, mobility, etc. the interfaces are also an important issue. The incompatible interfaces can cause stress formation, defect and interface states, surface recombination centers.

CHAPTER 3

SOLAR ENERGY AND PHOTOVOLTAIC SYSTEMS

The radiant heat and light energy from the Sun is called solar energy. In general, solar power describes the technologies that utilize sunlight to convert it into electricity or into heat. In this thesis, conversion of solar energy into electricity was taken into consideration, solely. Solar energy is non-intermittent and almost inexhaustible source of energy. According to the accurately done measurements, the average solar radiation power density outside the atmosphere of the Earth is 1366W/m^2, which is generally known as the solar constant (Fig. 3.1). By using the definition of meter, which refers to one over 10.000.000 of Earth's meridian, from North Pole to the equator, the radius of Earth is calculated as $(2/\pi) \times 10^7 m$. Then, the total power of solar radiation on Earth is calculated as,

$$\text{Solar Power: } 1366\left(\frac{\text{W}}{\text{m}^2}\right) \times \frac{4}{\pi} \times 10^{14} \cong 1.73 \times 10^7 \text{ W} \tag{3.1}$$

Now, the annual solar radiation reaching on the surface of the Earth can be evaluated by using the definitions of 365.2422 day in a year and the 86.400 s in a day,

$$\text{Annual Solar Energy: } 1.73 \times 10^7 (\text{W}) \times 365.2422 \times 86.400 (\text{s})$$

$$\cong 5.46 \times 10^{24} \text{J} \tag{3.2}$$

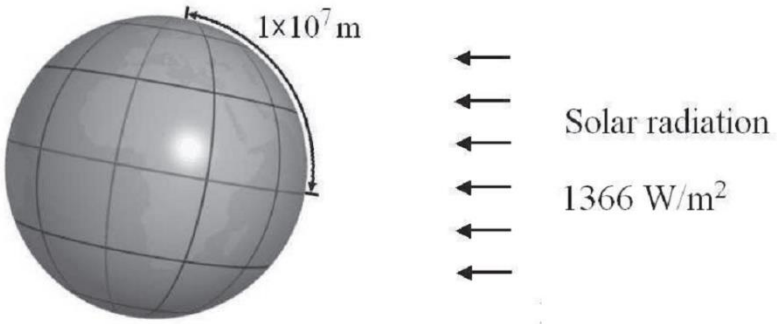

Figure 3.1. Annular solar energy arriving to Earth's Surface

To make a sense out of that amount of energy, comparing it with the annual global energy consumption is useful. Figure 3.2, represents the world energy consumption between 1990 and 2040 for the member countries of Organization for Economic Cooperation and Development (OECD) and nations outside the OECD (non-OECD). The world energy consumption was increased from 410 quadrillion Btu in 2000 to 524 quadrillion Btu in 2010 and the projections about this is the increment to 630 quadrillion Btu in 2020 and 820 quadrillion Btu in 2040 (quadrillion btu =1.05505585 × 10^{18} joules). As a result, it can be extrapolating that just 0.01% of the annual solar energy reaching Earth can satisfy the energy need of the entire world.

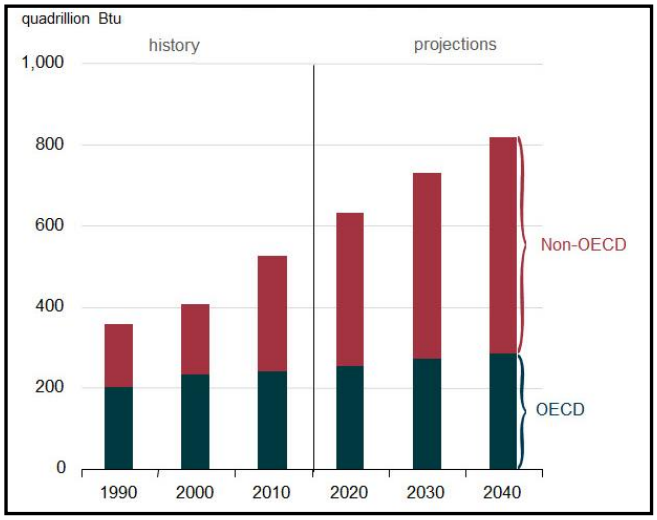

Figure 3.2. World energy consumption1990-2040
(Source: International Energy Outlook, 2013)

In addition, it should be explained that not all the solar radiation absorbs by the Earth. About 30% of solar radiation is reflected into space and about 20% of solar radiation is absorbed by clouds and by molecules in the air. Nevertheless, if only 10% of total solar radiation is utilizable, 0.1% of it can enough to meet the energy requirement in the world.

To meet the worldwide growing energy demand in green and in a cost competitive way, cheaper and handy clean energy systems are needed. Solar power is the most economic and powerful energy source among the other renewable energy sources. The more renewable energy will enable us to cut the greenhouse emissions and make it less dependent on imported energy. In addition, boosting the renewable energy industry will stimulate the technological innovation and employment. There are various types of renewable energy resources. Many of them have limitations, including hydropower, wind energy, and geothermal energy. Solar photovoltaics is the most promising energy conversion system that have potential to substitute for fossil energy.

3.1. Historical Overview of Photovoltaics

Photovoltaic (PV) systems are electrical power generating systems that capture sun energy and directly convert it into electrical energy. Such systems are the most powerful energy harvesting systems among the other renewable energy systems since the sun continually provides huge amount of energy on Earth. Although PV systems enable sufficient, green, non-polluting and low cost energy harvesting, their high production cost and low manufacturing capacity low the potential of these systems on the energy generation sector. Today, the systems in used to generate energy by renewable energies are biomass and wind power. Solar energy is the promise candidate for future power production, since it has ability to cover the global energy demand by itself. The high grow rates of PV market of 30-40% per year proves that enthusiastic interest in the investment in solar energy (Razykov et al. 2011). Since the most abundant energy resource available to human society is solar energy, the photovoltaic systems promise to be a major contributor of the future global energy demanding due to its minimal running costs, zero emissions and steadily declining module costs.

The term "photovoltaics" is the synthesis of two words; photo and volta. Photo is a Greek word that means light. It was integrated with the word volta to honor the Italian

physicist Volta, who had devised the battery in the 1800s. As a result, the term photovoltaics refers to light and electricity since 1849. During the late 1830s, a French physicist named Alexandre-Edmond Becquerel first recognized the photovoltaic process. While he was experimenting with an electrolytic cell made up of two metal electrodes placed in a conducting solution, he recognized an increment in the current measurements, after the experimental set up was exposing to light. After a numbers of experiments using several materials, he declared that electrical current in certain materials could be increased when exposed to light. However, it took long to translate that original thought to a device. In 1873, an English electrical engineer named Willoughby Smith, detected the photoconductivity of the element selenium. By this way, basis of photovoltaic cells was emerged. Shortly after that discovery, Smith recognized the photoelectric nature of selenium. Although, his attempts to build a solar cell was failed, the idea of producing electricity only by using solid material laid the foundation of solar cell.

An American inventor named Charles Fritts in 1883 built the first succeeded solar cell. He used the same idea with lies behind the conventional silicon solar cell of today. Fritts constructed a solar cell with thin wafers of selenium, which coated with very thin, semi-transparent gold wires to form a junction, and he used sheet glass as the protective layer (Fig. 3.3(a)). He achieved only 1% efficiency with this device. Nevertheless, he proved the feasibility of selenium based devices to produce energy by converting sunlight into the electricity.

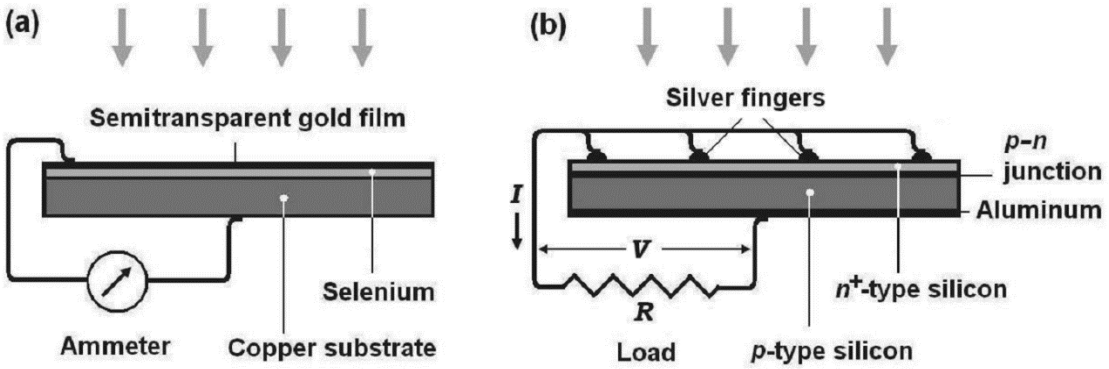

Figure 3.3. (a) Selenium solar cell (b) Silicon solar cell

In 1939, an American solid-state physicist Russell Ohl, discovered the crucially important phenomenon, p-n barrier in silicon at Bell Laboratory. While he was testing

the electrical resistance of a Si material, which had a crack on the middle, he noticed that he when the sample was exposed to bright light, the current that flowed between the two sides of the crack made a significant jump. Since the silicon atoms in the region on one side of the crack had extra electrons around them these two different parts of cracked Si material was yielded opposite electrical characteristics. These two distinct regions referred to p and n type regions; p-for the positive type, n- is for negative type region, which had extra electron around it. That behavior of cracked silicon was originated from the defects it had. Arrangement of atoms in the substance determined by the arrangement of electrons, which defines the physical, chemical and electrical properties of a solid. Therefore, understanding the electronic structure of the atom is crucially important. The main thing is how the conduction electrons are distributed in energy in a solid material. The impurities in silicon crystal caused some sections to resistant to current flow, thus it was the barrier between these two differ in purity. That barrier formed between these two different regions was called the p-n junction. That junction was acting like a barrier by preventing the excess electrons in the n-region from traveling over to the p-region, where atomic forces naturally dragged them. However, the situation was different when the silicon was exposed to light. Since the photon carries energy, when the light was striking this junction it stimulated electrons to flow across the junction. This results in as an electric current. As a result, defected Si material was behaving like a solar cell, that converting light into electric current. Ohl's discover led him later to develop the first silicon solar cell and had its patent in 1946 (Jones 2012). The Bell Labs scientists Daryl Chapin, Calvin Fuller, and Gerald Pearson develop the 6% efficient silicon solar cell in 1954. This silicon solar cell was based on controlled doped Si crystal. The n-side of the junction was highly doped and thin enough to allow light to come to the p-n junction easily, while the electric conduction is high enough to collect the current to the front contact through an array of silver fingers. The back side of the silicon is coated with aluminum film (Fig. 3.3(b)) (C. J. Chen 2011).

R&D is not only focusing on enhancing the conversion efficiency and the stability of the solar cells, but is also trying to find processes and technologies to reduce the costs. Flexible CZTS solar cells are therefore very attractive because of their high conversion efficiencies, their low cost potential and the many application possibilities.

3.2. Basic Concepts of Photovoltaics

Photovoltaic cells are advanced semiconductor devices that directly converts solar energy into the electrical energy when it is exposed to sunlight. The sunlight is composed of photons with various amounts of energy that corresponds to the different wavelengths of the solar spectrum. The solar spectrum contains photons with energies ranging from 0.5 to 3.5 eV. Only the absorbed photons generate electricity. Photons with energies below the semiconductor band gap are not absorbed and does not contribute to current and to efficiency. The conversion efficiency of a solar cell is the proportion of sunlight energy that the cell converts to electrical energy. Since the current flows in one direction and the electricity generated is termed direct current. Before giving the detailed explanation of operation principle of photovoltaics, some basic concepts related with the theory of solar cells will be introduced in this section of the thesis.

3.2.1. Standard Illumination Conditions

Changing the light intensity incidents on a solar cell changes all solar cell working parameters. Therefore, in order to compare the efficiencies of solar cells, some standard test conditions have been designed

Solar radiation considered as a black body radiator at definite temperature. Throughout the path, which sunlight takes at atmosphere until it received on Earth, it interacts with several chemicals through this path and it is scattered and in some cases absorbed by these chemicals at certain wavelengths. As a result, mostly the spectral range between the far infrared and near ultraviolet reaches to the Earth's surface.

The air mass coefficient (AM) is used to determine the standard illumination condition of solar cells. The AM followed by a number and it refers the ratio of a path length (L) of sunlight through the atmosphere, to the path length vertically upwards, zenith length (L_0) (at sea level). AM 1.5 is standard for characterizing terrestrial solar cells. For AM 1.5, z (zenith angle) is 48.2^o

$$AM = \frac{L}{L_0} \approx \frac{1}{\cos z} \tag{3.3}$$

The other standardized conditions in determining the efficiency of the solar cells are 1000 W/m^{2}intensity, 25°C ambient temperature.

3.2.2. Fill Factor

The Fill Factor (FF) is essentially determines the performance of the solar cell. The typical value of FF is between 0.8 and 0.9. It is equate with the ratio of the solar cells maximum actual power output (V_{max} x I_{max}) versus the power product V_{oc} x I_{sc} (Fig. 3.4).

$$FF = \frac{P_{max.}}{V_{oc} \times I_{sc}} \tag{3.4}$$

In the Equation 3.4, V_{oc} refers to open circuit voltage. It is the voltage between the terminals of a solar cell under standard illumination conditions when the load has infinite resistance (zero current). The other denominator term, I_{sc} refers to short-circuit current. It is the current of a solar cell under standard illumination conditions when the load has zero resistance (zero voltage). Since the power is P=IV, the P_{max} in the numerator is determined by the condition

$$dP = d(IV) = IdV + VdI = 0 \tag{3.5}$$

The FF can be illustrated graphically in the IV curve of the solar cell, it is the largest rectangle which will fit in the IV curve (Fig. 3.4).

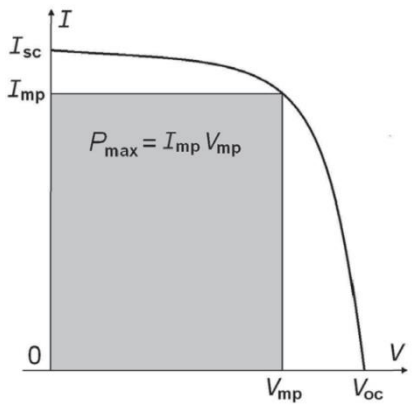

Figure 3.4. Maximum power and fill factor

3.2.3. Efficiency

Energy conversion efficiency (η) of a solar cell is the percentage of the electrical power it delivers to the load ($P_{max.}$) to optical power incident on the cell by the absorbed photons ($P_{inc.}$). The highest efficiency achieved when $P_{max.}$ is maximum. Incident optical power is estimated through the standard illumination conditions.

$$\eta = \frac{P_{max.}}{P_{inc.}} = \frac{V_{oc} \times I_{sc} \times FF}{P_{inc}} \tag{3.6}$$

3.2.4. Peak watt

The term peak watt (W_p) refers to the power (in watts) of a solar module produced by the solar module, under standard illumination conditions at the maximum incident power point.

3.3. Types of Solar Cells

Among the other renewable energy sources, solar energy is the most efficient renewable energy source with its high capacity easy installation facility since it has no moving parts. Operational principle of photovoltaic systems is grounded on three basic components. The first of them is the electron-hole pair creation when the sunrays absorbed by the p-type semiconductor layer that so-called absorber layer. The second one is the electron-hole pair separation in the p-n junction. The last one is the transmission of these mobile electrons means flow of current through the external circuit with the help of back and front conductive contacts. Operation principle of all semiconductor devices is based on the controlling the flow of electrons in a semiconductor material which is a crystalline solid.

In general, types of solar cells can be grouped through their junction properties;

- Homojunction device; electrical properties of a single material is altered by doping it, in order to obtain two distinct parts within the material up to be p- and n-type. Since the p-n junction is located, the maximum amount of light absorbed near it. Example; crystalline silicon (c-Si) solar cells

- Heterojunction device; Two different semiconductor material with distinct electrical characteristics are used to form the p-n junction. The p-type layer (bottom layer) material has low bandgap to absorbed high amount of light. The n-type layer (top layer) material has high bandgap is favorable for its transparency property. Example; CdTe, $CuIn_xGa_{1-x}(Se,S)_2$, Cu_2ZnSnS_4 based solar cells
- p-i-n and n-i-p devices; Three layered sandwich model is created in these devices which an intrinsic semiconductor is between n-type and p-type layers. The generation of electron-hole pairs takes place in this intrinsic layer. Example; a-Si:H solar cells.

The c-Si solar cell was the first homojunction solar cell. There are two versions of silicon solar cells; single crystalline and polycrystalline. The efficiency of monocrystalline silicon solar cells is 14–20%, for large-scale solar cells, which is still the highest in homojunction solar cells. Since this is a robust and proven technology, today's mainstream photovoltaic industry is based on C-Si wafers. However, due to the high cost manufacturing of silicon wafers, possible cost reduction potential in this industry is limited. On the other hand, thin film a-Si:H solar cells are much less expensive compare to crystalline ones, yet the efficiency is only 6–10%.

The most efficient solar cells reaching a record of 43.5% conversion efficiency under concentrated light achieved with multijunction solar cells (Wiemer et al.). In tandem solar cells, each cell is optimized to achieve maximum voltage for different wavelengths of the solar spectrum. The large difference in the bandgap values enables much better utilization of the solar spectrum. However, its high cost production limited its fabrication to satellite and space applications.

To provide solar energy to be a widespread renewable energy source, it should be produced in a cost effective fashion. There are several different approaches in order to make photovoltaic technologies to be cost competitive with other power sources. PV markets in Europe and around the world continued making rapid progress in 2012 toward competitiveness in the electricity sector. The decrement in the prices of solar technology, and increased electricity prices around the world helped to achieve this success.

Thin film solar cell technology is a promising technology for terrestrial and space applications since it offers a wide range of options in device design and fabrication technique. First, thin film technology enables cheap manufacturing and cheap material usage.. Furthermore, opposite Si technology, a variety of substrates such as flexible or rigid, metal or insulator can be used to deposit component layers on it by using vari-

ous thin film deposition techniques (PVD, CVD, ECD, etc.). Such versatility enables engineering and designing of the layer to improve the device characteristics and performance. Thin film solar cell technology has potential for fabrication cheaper devices on large scale.

3.4. Thin Film Solar Cells

The c-Si solar cell technology, which is the dominant technology in photovoltaic market, relies on the indirect bandgap absorber material. As a result, it requires a thick layer to absorb more fractions of the incident solar radiation. The thin film materials overcome the C-Si in that they have direct band gaps. This means, their absorption coefficients are high and thereby, so much thinner film of materials is enough to collect the same amount of light.

There is large number of possible thin film materials to be used in solar cells. Thin film inorganic solar cells mostly based on cadmium telluride (CdTe), copper indium gallium diselenide (CIGS) and a-Si:H materials. Usage of these compound materials significantly reduced the cost for fabrication of solar cells, also relatively high efficiencies are achievable. Due to greatly reduced semiconductor material consumption and feasibility for fabrication on inexpensive large –area substrates make thin film solar cell technology preferable. Doubtlessly, the thin film solar cells will play an important role for sustainable energy supply in the near future.

Though by using Si as a solar cell material, high efficient cells have achieved, intrinsically it has a disadvantage. Since Si is indirect bandgap semiconductor, the absorption coefficient near its band edge is low. As a result, thick Si wafer substrate is needed to achieve an adequate absorption of light. That disadvantage causes Si cells to be expensive in the cost of material and in the cost of mechanical processing.

The type of the energy bandgap affects the efficiency. The photon can directly excite an electron from valance band to the conduction band without a change in its momentum in direct bandgap semiconductors such as GaAs, $CuInSe_2$, CdTe etc. This results typically greater absorption coefficient for this semiconductor compounds, that is greater than $1\times10^4 cm^{-1}$. Figure 3.5 illustrates the absorption spectra of commonly used semiconductor solar cell materials. Table 3.1 lists the physical properties of these materials. To absorb high amount of photon for direct bandgap semiconductors the required

thickness range varies from a few nanometer to a few micrometers for thin film solar cells while a thickness of at least 50 μm is required for efficient absorption in indirect bandgap semiconductors.

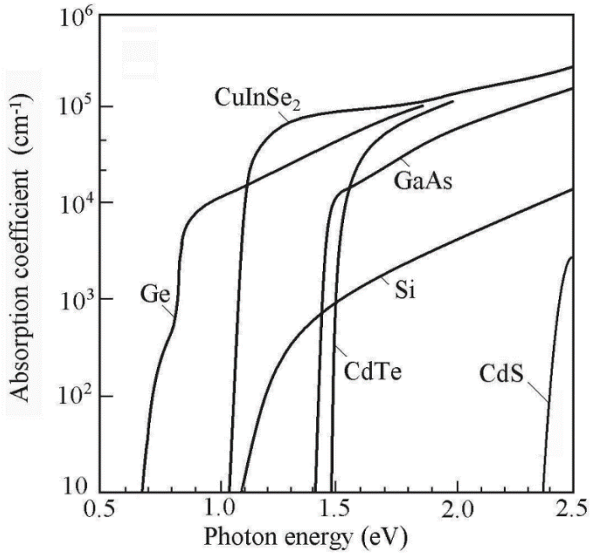

Figure 3.5. Absorption spectra of semiconductors commonly used for solar cells

Table 3.1. Physical properties of common semiconductor solar cell materials

Material	**Ge**	**$CuInSe_2$**	**Si**	**GaAs**	**CdTe**
Type	Indirect	Direct	Indirect	Direct	Direct
Bandgap(eV)	0.67	1.04	1.11	1.43	1.49
Absorption edge (μm)	1.85	1.19	1.12	0.87	0.83
Absorption coef. (cm^{-1})	$5.0x10^4$	$1.0x10^5$	$1.0x10^3$	$1.5x10^4$	$3.0x10^4$

Photovoltaic materials are inorganic semiconductor materials that form junctions with opposite type semiconductor material and exhibit a photovoltaic effect when light shines on it. Even though large number of semiconductor materials exhibits photovoltaic effect, only a few of them are commercially available in the market. Utilization of elemental materials is simpler, but there are no suitable elemental semiconductor available with direct bandgap close to 1.5 eV (Table 3.1). To date, besides silicon, only two such materials have reached the status of mass production. These are CdTe and CIGS based polycrystalline thin film solar cells.

An alternative to the inorganic semiconductor absorber material is the organic semiconductors. Unlike the creating free electron-hole pairs in inorganic semiconduc-

tors when expose it to light, bound electron-hole pairs (excitons) with binding energy of 0.5eV are created in organic solar cells. These excitons carry energy (no net charge) and they have to diffuse to dissociation sites to be separated and flow through the contacts. The light absorption is relatively low in organic semiconductors since their bandgaps are larger than 2.2 eV. Means, additional layers to trap light is necessary for organic solar cell devices.

3.5. Structural Properties of Polycrystalline Thin Films

Thin film technology offers wider choice of photovoltaic materials exist in two-component alloy or compound films. A metastable alloy film of a-Si:H is an attractive material with a tailorable bandgap, easy dupability and high optic absorption coefficient. It is seem like a good substitution for C-Si since its significantly reduced cost compared to C-Si. However, its overall efficiency and stability are lower than that of their crystalline counterpart. Due to the Staebler-Wronski effect known as light-induced degradation in amorphous silicon. The defect density of a-Si:H increases by the light exposure and as a resulti recombination rate increases and efficiency decreases. Beside this metastable a-Si:H alloy, other binary compound semiconductor materials are attractive for thin film solar cells, such as GaAs, InP, CdTe, etc. Even though very high efficiencies are available with GaAs and InP, they are so much expensive to use in high throughput manufacturing. With increasing the number of constituent elements, the number of possible photovoltaic materials can be increased. For example, alloys and compound of I-III-VI ($CuInS_2$) ternaries,and isoelectronically correlated quaternaries, named chalcopyrite materials, are widely used as absorber material in thin film solar cells.

3.5.1. Chalcopyrite Structures

The chalcopyrite structure is very similar to the diamond or sphalerite (ZnS) structures. Sphalerite structure is based on inscribing a tetrahedral in a face-centered cube. Chalcopyrite structure is as doubled sphalarite structure means, it has a tetragonal crystal system. Many compounds of composition I-III-IV_2 or II-IV-V forms in the chalcopyrite crystal structure. It can be visualized as; these three constituents are placed on

the sites of diamond cubic structure, with a small distortion due to the loss of symmetry involved. The anions are placed on one of the fcc sublattice of the diamond cubic structure, while the cations share the other one. The alloy $CuInS_2$ belongs to the group of ternary chalcopyrite compounds. It derives from group IV tetrahedrally bounded semiconductors (Si) according to the Grimm-Sommerfeld rule. This rule says there must be an average of four valance atoms per atomic site. From the group IV semiconductor, binary sphalerite structure forms (ZnS, GaAs), and chalcopyrite structure ($CuInS_2$, $CuGaSe_2$) derives from the sphalerite structure.

The $Cu(In,Ga)(S,Se)_2$ structure is a p-type semiconductor compound. By changing the atomic ratio of the group III elements In and Ga, the compound changes and as a result, the band gap of the material changes from 1.01 eV ($CuInSe_2$) to 1.68 eV ($CuGaSe_2$). Furthermore, the band gap of the compound can be engineered by changing the VI group elements S and Se contents in the compound, from 1.01eV ($CuInSe_2$) to 1.53 eV($CuInS_2$) or from 1.68 eV ($CuGaSe_2$) to 2.43 eV ($CuGaS_2$) (Maeda, Takeichi, and Wada 2006). Chalcopyrite material considered as an ideal photovoltaic material with bandgap optimum bandgaps, but the difficulties in controlling sulfur diffusion into metals and impurity species, slows down the evolution of this material. However, efficiencies over 20% have obtained with CIGS material (Jackson et al. 2011).

A typical chalcopyrite-type thin-film solar cell consists of a p-type, chalcopyrite-type absorber, and an n-type transparent window layer, which together form a p-n junction. The window layer consists of a CdS buffer layer and a ZnO front contact.

3.5.2. Kesterite CZTS Structure

Cu_2ZnSnS_4 abbreviated to CZTS is p-type semiconductor with a direct band gap of in the range 1.4-1.5 eV. CZTS is highly suitable absorber layer material for thin film solar cell due to its high absorption coefficient of more than 10^4 cm^{-1} (Ito and Nakazawa 1988). CZTS is derived from the chalcopyrite CIGS structure by the isoelectronic substitution of the two group III atoms (In or Ga) by one Zn and one Sn atom. Therefore, CIGS and CZTS materials have similar properties, consequently. CZTS is a quaternary compound semiconductor of $(I)_2$-(II)-(IV)-$(VI)_4$.

Since this compound only consists of abundant elements with low toxicity levels, CZTS, in order to avoid the problems related to CIGS like the limited Earth abun-

dant In, Ga and toxic Se, so many research groups have turned their attention to this newly explored quaternary compound semiconductor.

The crystal structure of CZTS is refered to as kesterite (space group I4) and can be derived from the sphalerite structure by duplicating the unit cell. During the formation of CZTS, CZTS can crystalizes in kesterite or stannite structure (Fig.3.6). The only difference between the kesterite and stannite structure is the different ordering of cation sub-lattice. As shown in Figure 3.6., in kesterite CZTS crystal, CuSn, CuZn, CuSn and CuZn cation layers alternate at z = 0, ½, ½ and ¾, respectively. For Stannite CZTS crystal, ZnSn layer alternate with Cu_2 layers (Paier et al. 2009). Since the negative formation energy of kesterite structure is lower than stannite structure, the kesterite structure was found to be the most stable phase of CZTS (Maeda et al. 2011).

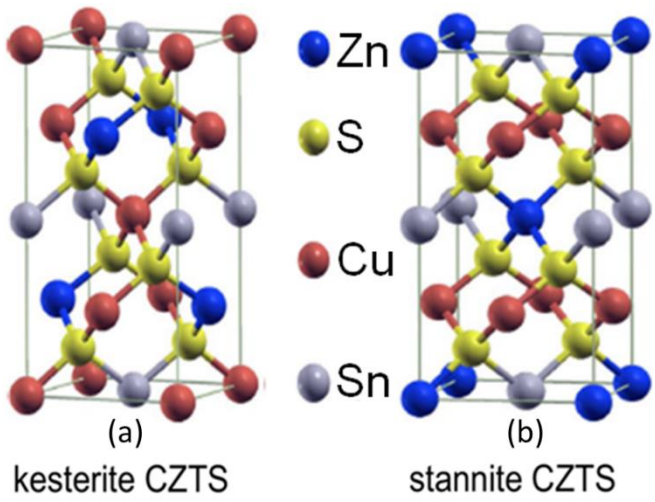

Figure 3.6. Crystal structures of (a) kesterite, (b) stannite CZTS

CZTS is a self-doped p-type semiconductor compound due to the formation of intrinsic point defects including vacancies (V_{Cu}, V_{Zn}, V_{Sn}, and V_S), antisite defects (Cu_{Zn}, Zn_{Cu}, Cu_{Sn}, Sn_{Cu}, Zn_{Sn}, and Sn_{Zn}), and interstitial defects (Cu_i, Zn_i, and Sn_i) (Chen et al. 2010). This random nucleation during growth of CZTS leads desired properties to have proper electrical characteristic to be used in thin film solar cell device as an absorber layer. It was found that formation energies of acceptor defects were lower than donor defects. Especially, commonly observed Cu_{Zn} anti-site defect, which an Cu atom Zn atom exchange sublattices, leads to p-type conductivity for CZTS semiconductor material. Means, obtaining CZTS material deviated from stoichiometric ratio, with Cu-poor, Zn-rich compositions, enables to obtain desired electrical properties in CZTS ma-

terial. However, this deviation from stoichiometry leads to undesired second phase formations. These secondary phase formations can be investigated by phase diagrams. In Figure 3.7, a ternary phase diagram is shown. This ternary phase diagram was developed (Scragg 2010) by using the basis of the research by Olekseyuk *et al*. Even though CZTS is a quaternary compound, by assuming to always get right amount of sulfur in samples, the phase diagram can be degraded to three constituent (Flammersberger 2010).

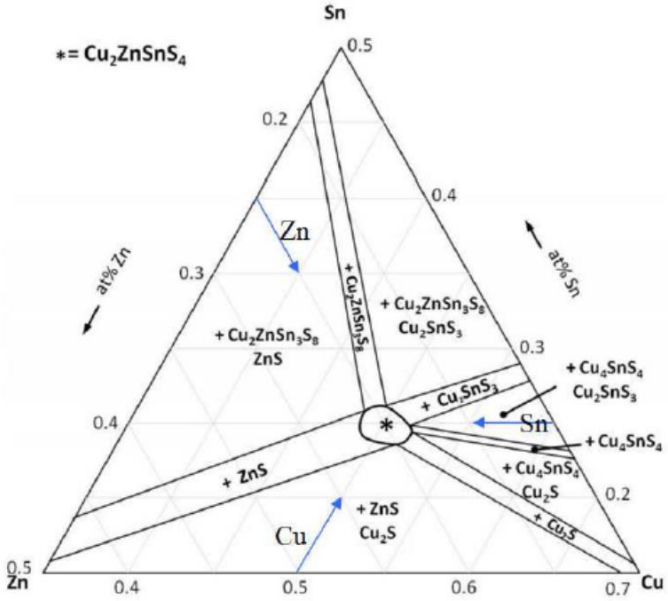

Figure 3.7. Ternary phase diagram of CZTS

In this diagram, each field represents CZTS formation addition to the related second phase formation, depending the atomic composition of associated element, within it. There are ten field in this diagram that shows the feasibility of second phase formation is high. The eleventh region in the middle, marked with a star, is where the pure CZTS formation is possible.

Formation of these secondary phases has a big impact on the device characteristic. Second phases with metallic character, such as Cu_2S and ternary Cu_2SnS_3, cause shunt paths in device. These are the most detrimental second phases for device efficiency. KCN etching help to remove Cu_2S and Sn related undesired phases from the CZTS material. n-type semiconductor SnS_2 second phase formation takes place in Sn-rich regions. It acts as an insulator due to its large bandgap. The other insulator second phase

is ZnS, which forms in Zn-rich, Cu and Sn poor regions. It inhibits the current flow and reduces the possibility of electron-hole pair formation possibility in absorber layer.

Currently, efficiencies up to 9.2% and 12.6% have been achieved for the kesterite structures Cu_2ZnSnS_4 (Hiroi et al. 2013) and $Cu_2ZnSn(S,Se)_4$ (Wang et al. 2014), respectively. Theoretical calculations based on the Shockley-Queisser limit for a single p-n junction with a band gap of 1.4 eV claim that an approximately 33.7% maximum solar conversion efficiency can be generated (using an AM 1.5 solar spectrum) (Shockley andQueisser, 1961). For these reasons, the CZTS compound semiconductor will be the preferred material for thin-film PVs in the immediate future.

3.6. Solar Cells on Flexible Substrates

In principle, we differentiate between two categories of flexible substrates: polymers and metal foils. The used polymers are usually special heat resistant polyimides (PI), like Upilex or Kapton. Nevertheless the highest temperatures, they can withstand, are around 450° - 500°C, which is still ~100 K lower than usual deposition temperatures on glass. The metal foils (stainless steel, Ti, Cu, Mo, etc.) on the other hand can be used at higher temperatures without any deterioration of the substrate, but have to deal with other problems. One is the diffusion of impurities from the substrate into the absorber layer, which have negative effects on the photovoltaic properties of the solar cells. That an additional barrier layer between the substrate and the back contact is needed to eliminate or reduce it to such low impurities diffusion, so that it does not harm the solar cell properties anymore. Additionally the diffusion barrier can be used, if the layer is not conductive, for a second purpose at the same time. It can make an electrical isolation of the devices from the substrate in order to perform monolithical integration for modules. Nevertheless, all those buffer/barrier layers should withstand high temperature processing. Any cracking in these layers can be detrimental.

Empa recently published a new world record in efficiency of 18.7% on polyimide foils (Reinhard et al. 2013). The 18.7% cell not only shows the highest efficiency value on polyimide, but also the best performance compared to any published result on flexible solar cells. Efficiency 17.3% was obtained using a Mo back contact with a thin Ti adhesion layer, in combination with a low-temperature CIGS deposition process with

no additional oxide or nitride impurity diffusion barrier layer on stainless steel foils (Blösch et al.).

In case of plastic substrates, the shrinkage and elongation by gas permeation through plastic are a main issue. Therefore, a gas barrier is necessary to protect the device from the penetration of moisture to the plastic, which is not needed for metal foils, such as stainless steel and Mo foils. In addition, substrates such as plastics can be damaged during high-temperature processing. On the other hand, in case of Mo foils, the process temperature can be higher than 1000 ^{o}C because of its high melting temperature of 2610^{o}C.

Metallic foils, such as Cr-steels, titanium, molybdenum, aluminum and some alloys are promising flexible substrates because they are cheap, lightweight, durable, and resistant to high-temperature fabrication processes. Additionally, metallic flexible substrate utilization eliminates the need for the deposition of a metallic conductive back contact layer. As a result, the cost of manufacturing and constructing solar cell modules would be substantially lowered. The preferential flexible substrates should have well-matched CTE (i.e., 5–12x10^{-6} K^{-1}), sufficient thermal (T ≥400°C) and chemical resistivity (especially against S and Se), and should be suitable for roll-to-roll deposition, in addition to being cost efficient.

Growth of CZTS layer on the flexible Mo foil has only been investigated via the solvothermal approach (Dai et al. 2012). Deposition of CZTS layers on flexible polyimide substrates were carried out using a screen printing process (Zhou et al. 2010) and electrochemical deposition technique (Farinella et al. 2014).

Chemically inert back contact layer with optimum electrical characteristics is a requirement to achieve high efficient solar cell. In the case of Mo back contact, high temperature sulfurization process leads to decomposition of the CZTS absorber layer and results in the formation of MoS_2 phase (Scragg et al. 2012), (Scragg et al. 2013). The interfacial MoS_2 layer may affect the V_{oc} and change the band alignment between the CZTS absorber layer and Mo substrate. A back-contact blocking barrier is formed, which restricts the transport across the CZTS to Mo layer (Yang et al. 2014).

Furthermore, impurities released from the substrate are another problem in the case of metal foil utilization. Among the appropriate metal foil substrates, the pure metallic foil substrates like chromium and titanium can be used without a diffusion barrier since their diffusion rates into the absorber are comparably low (Hartmann et al. 2000) and have no detrimental effects on the conversion efficiency of the solar cells.

Other intrinsic physical properties of the substrate such as the CTE and surface roughness affect the properties and structural characteristics of the adjacent active layer. The CTE of the substrate and the adjacent active semiconductor layer should be in the same range. The adhesion problems may occur due to the high CTE of the substrate while the defects like crack formation may take place due to low CTE of the substrate. Formation of cracks decreases the performance of the device since it creates shunt paths between the back and front contacts of the device. Micro-cracks are also inactive cell domains and thus, they reduce the active cell area. Therefore, back contact with nearly equal thermal expansion coefficient of absorber layer is preferable to reduce the possibility of crack formation. Additionally, since surface roughness of the metal substrate causes leakage current and pinholes, surface smoothness of a metallic substrate is another important factor to achieve high efficient flexible solar cells (Yagioka and Nakada 2009), and smooth surface may ensure easier and more homogenous active layer deposition.

Furthermore, the choice of substrate is crucially important to reduce the manufacturing costs for the high throughput fabrication of thin film solar cell. The costs of commercially available metal foils depends on the purity level and the Earth's reserve of the element. The abundance on Earth's crust of Ti and Mo elements are 0.66% and 0.00011%, respectively. Consequently, Mo foil is much more expensive due to its lower abundance than that of Ti foil.

The objective of this study is to establish a clear understanding of the substrate and back contact behavior of these promising Ti and Mo flexible substrates.

CHAPTER 4

EXPERIMENTAL PROCEDURES

In the present work, magnetron sputtering technique was used in the first stage of the growth mechanism since sputtering offers a wide range of advantages, such as easy adaptation to large-scale and reproducible manufacturing. Additionally, we chose to study both with Ti and with Mo foil substrates, due to the preferable CTE and chemical inertness behavior of Ti, and also Mo foil was used to compare the results those of Ti foil. Additionally, soda lime glass (SLG) substrate was used to make optical and electrical characterizations of grown CZTS semiconducting layers. Table 4.1 lists the growth parameters of samples will be discussed through this thesis.

Table 4.1. Table of growth parameters of discussed samples

	Substrate	**Layer Ordering**	**Sulfurization Temperature**	**Sulfurization Duration**
CZTS-32	SLG	Cu/Sn/Zn/Cu/Sn/Zn	560	2 hours
CZTS-36	Ceramic	Cu/Sn/Zn	570	2 hours
CZTS-58	Ti foil	Cu/Sn/Zn/Cu/Sn/Zn	560	2 hours
CZTS-63	Mo foil	Cu/Sn/Zn/Cu/Sn/Zn	570	2 hours

4.1. Substrate Preparation and Pretreatment

Flexible substrate usage results in many advantages compared to that solar cell fabricated on soda lime glass. CZTS absorber layers have been fabricated on two types of metallic foils; Ti and Mo foils. It is well known that substrate roughness of foil substrates is one of the most important issues to achieve high-efficiency flexible CZTS solar cells. As-purchased metal foils have rough surface arising from the foil production process. In order to get rid of the textured surface of foils, polishing or coating by a levelling layer are the necessary steps in the case of foil substrate utilization (Kessler and Rudmann 2004). Before the sputtering process, to remove the oxidized layer and to decrease the surface roughness, the Ti and Mo foils were chemically etched with diluted

HF and HCl, respectively. Surface roughness of Ti and Mo foils were examined by AFM spectroscopy before and after etching with diluted HF and HCl, respectively.

Additionally, a passive oxide film is spontaneously formed on Ti surface when exposed to air at room temperature. This passive film forms in amorphous structure and is composed of three layers; firstly TiO forms adjacent to metallic titanium, then Ti_2O_3 layer and the third layer contact with the environment is anatase TiO_2 layer (Pouilleau et al. 1997). This amorphous oxide film crystallizes into anatase at about 276 ^oC, stays in anatase stucture in the range of 276-457 ^oC and contains both anatase and rutile sublayers in the range of 457-718 ^oC (Gemelli and Camargo 2007). Since this intervening oxide layer is detrimental to create an ohmic contact between the CZTS and Ti metal substrate, we aimed to etch this amorphous passive oxide layer before sputtering, since sulfurization process requires heat treatment higher than 500 ^oC.

A mixed acid solution treatment is a frequently used surface treatment method to remove oxide layer and contaminations from the surface. It is well known that, TiO_2 is the dominant oxide layer formed on Ti surface due to its high affinity to react with O_2. Prior to the other surface treatments on Ti surface, these oxide layers should be removed. There are five acid solutions in use to remove oxide layer from Ti surface. A standard acid solution is composed of HF and HNO_3 or only HF in distilled water (Walker and Tarn 1991). Takeuchi *et al*. studied three other solutions; $Na_2S_2O_8$, H_2SO_4, and HCl to see their decontamination efficiencies on Ti surface. We have chosen HF solution in distilled water for the removal of oxide layer from Ti foil. Our studies revealed that oxide phase removal has succeeded using HF in distilled water. . To ensure the removal of the oxidized layer, CZTS deposition on untreated Mo foil and Ti foil samples were analysed and compared with etched foil samples.

4.2. Metallic Precursors Fabrication

In the first stage of the process, Cu-Sn-Zn metallic layers were deposited by using a multi-target magnetron sputtering system (Figure 4.1(b)). As the metallic foil substrate, 100 μm thick and ≥99.9% trace metal basis Ti and Mo foils supplied by Sigma-Aldrich were used. Before the sputtering process, Ti and Mo foils were chemically etched with diluted HF and HCl to remove the oxidized layer and to decrease surface roughness. The Raman spectroscopy analysis verified that there was not any trace of

oxidized layer upon foils. Additionally, Ti and Mo thin film coated Sinterflex ceramics were as a part of the TUBITAK-1002 project studies. Furthermore, SLG substrate was used to investigate the electrical and optical characteristics of the CZTS material. The CZTS layers were grown on these substrates via sulfurization of the stacked metallic precursors that were deposited sequentially by multi target dc magnetron sputtering from 2-inch-targets of Cu (99.999%), Zn (99.99%), and Sn (99.999%) at room temperature.

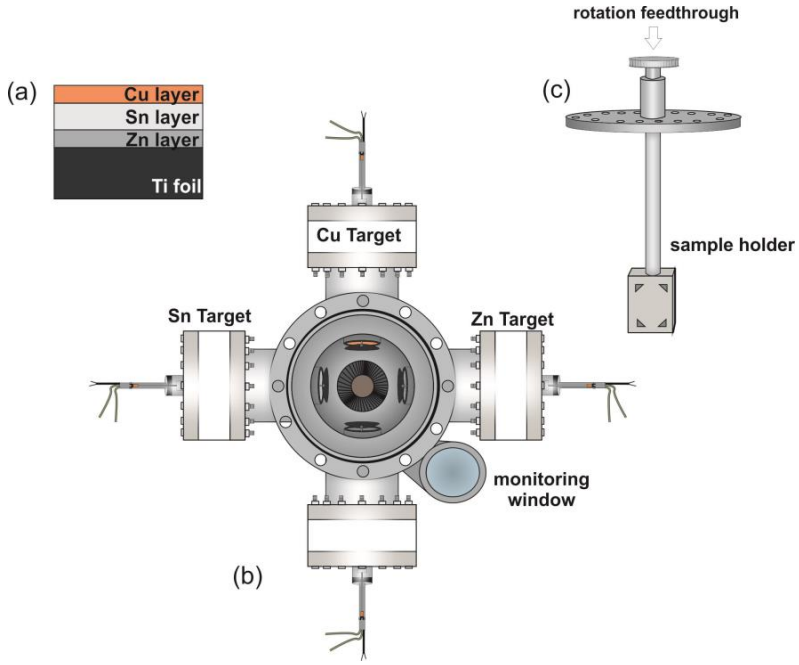

Figure 4.1. (a) Illustration of Ti foil substrate sample (b) Schematic diagram of top view of multi-targeted sputtering system (c) Illustration of sample holder apparatus, within the sputtering system

After base pressure was reached below 10^{-6} torr, the sputtering procedure was started. Operating pressure was maintained at $1.5x10^{-2}$ torr, and target-to-substrate distance was fixed at 8 cm. In this way, we grow sequentially layered metallic precursors in the different layer ordering on Ti and Mo foils, also on ceramic and SLG substrate (Fig. 4.2).

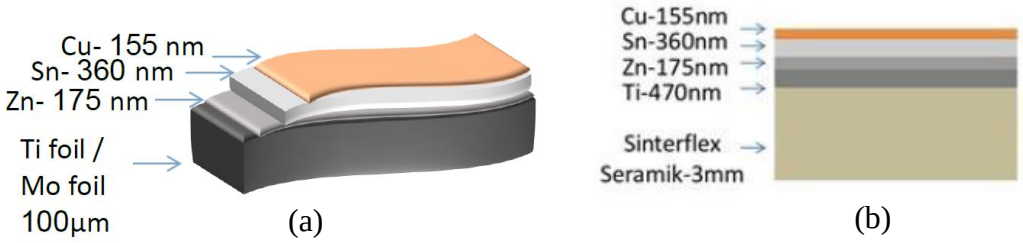

Figure 4.2. Schematically illustrated samples on a (a) flexible foil, (b) Ti coated ceramic substrates

Magnetron Sputtering Technique:

There are many different ways to deposit thin film layers onto a substrate. Thin film deposition techniques can be grouped into two types as vacuum-based and nonvacuum techniques. During the experimental work of this present thesis, magnetron-sputtering method, which is a vacuum-based technique, was used.

Sputtering is physical vapor deposition technique used for deposition thin film layers onto a chosen substrate, by ejecting atoms from target material and condensing the ejected atoms onto that substrate under high vacuum environment.

A target material that is desired to be obtained in thin film layer, is bombarded with energetic ions, typically inert Ar gas ions (Ar^+) are used for this purpose. Electrically neutral Ar gas introduces into sputtering chamber at pressure of 1to10 mTorr. A DC voltage supplier is placed between the target and substrate which ionizes the Ar atoms and creates plasma, glow discharge consisting ions and electrons. These energetic Ar^+ ions are accelerated towards to cathode target to collide with the target atoms. In this way, target atoms ejected from the surface. These ejected target atoms then reach to substrate and condensed on it. During Argon ionization released electrons are accelerated to target as well, subsequently colliding with additional Ar atoms. Therefore, more ions and free electrons participate to process. As more and more atoms are ejected and condensed on the substrate, they begin to bind to each other at the molecular level, forming an atomic layer. Number of layers, means thickness of the thin film, depends on the sputtering power and time.

This mentioned process covers the operational principle of DC sputtering. The main difference between DC and magnetron sputtering is, addition the system described above, a strong magnetic field takes place near the target area by using magnets. This field causes travelling free electrons to spiral along to magnetic flux lines in the vicinity

of target surface, instead of being attracted towards anode. The advantage of this is that the plasma confine into an area near to target. Hence, plasma damage cause by the stray electrons and Ar ions, to deposited film is suppressed. Furthermore, the mean free path of the electron is elongated and the probability of colliding with an Ar atom is increased. This results in, more dense and stable plasma. Density of plasma is proportional with the present ions and more ions mean high deposition rate in the process. High deposition rate minimizes the impurity formation during atomic layer formation substrate.

4.3. Annealing Process

The second stage of the process is sulfurization of the metallic precursor. The sulfurization procedure was performed in a Lindberg/Blue M tube furnace. We used a homemade specially designed quartz glass tube, which has a little cylindrical outward partition, to put the sulfur powder (99.98%) in it. That cylindrical partition was heated to around 130 ^{o}C via Joule heating for formation of sulfur vapor. This system, enabled precursors to be heated quickly by transferring precursor from the room temperature zone to furnace central zone using a transfer rod (Fig. 4.3). Metallic precursors were loaded in the quartz tube installed in the tube furnace. Using a MKS 647C mass flow controller, Argon (Ar) gas flow was directed into the quartz tube as the carrier gas during the sulfurization stage. The different sccm values were investigated during the calibration process. Finally, it was found that, by sending 100 sccm Ar through the sample that was placed in the tube furnace, the best result was achived. Ar gas selected as the carrier gas instead of N_2 gas, since formation of TiN interface layer might be deteriorating the CZTS formation on foil substrate. The pressure was maintained at the atmospheric level. Figure 4.4 represents the illustration of the sulfurization process.

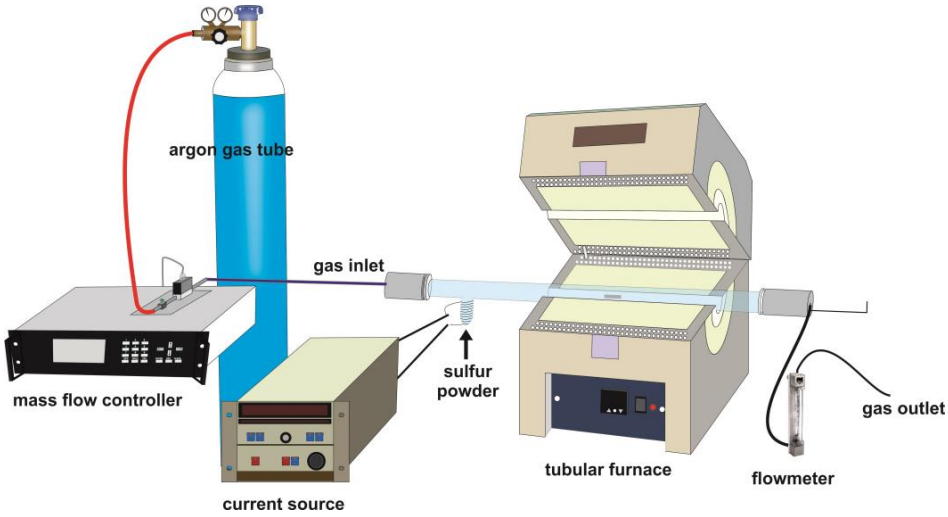

Figure 4.3. Illustration of annealing set up

We first set the furnace from room temperature to 270 ^{o}C and we pushed the metallic precursor into the furnace using the transfer rod. The furnace temperature was raised to 560 ^{o}C with the increments of 10 ^{o}C per minutes. Figure 4.5, represents the sulfurization process parameters of CZTS films for this study. After two hours of sulfur treatment, the current source was turned off and just Ar gas inlet was on. Afterwards, the films were cooled naturally. We used this sulfurization parameter after large number of calibration work. We investigated lower sulfurization temperatures and shorter sulfurization durations. The effects of sulfurization temperature and duration will be discuss in Chapter 5. Results and Discussion.

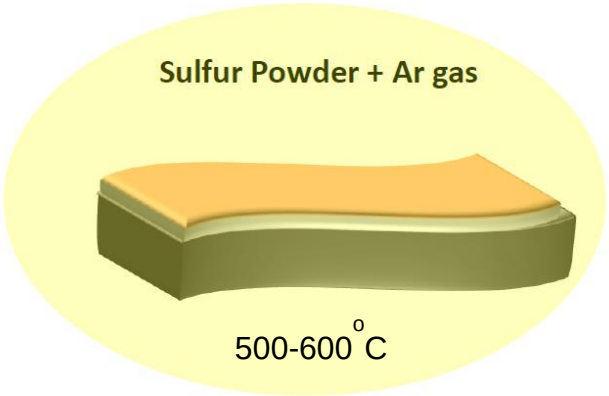

Figure 4.4. Schematic demonstration of sulfurization process of metallic precursor

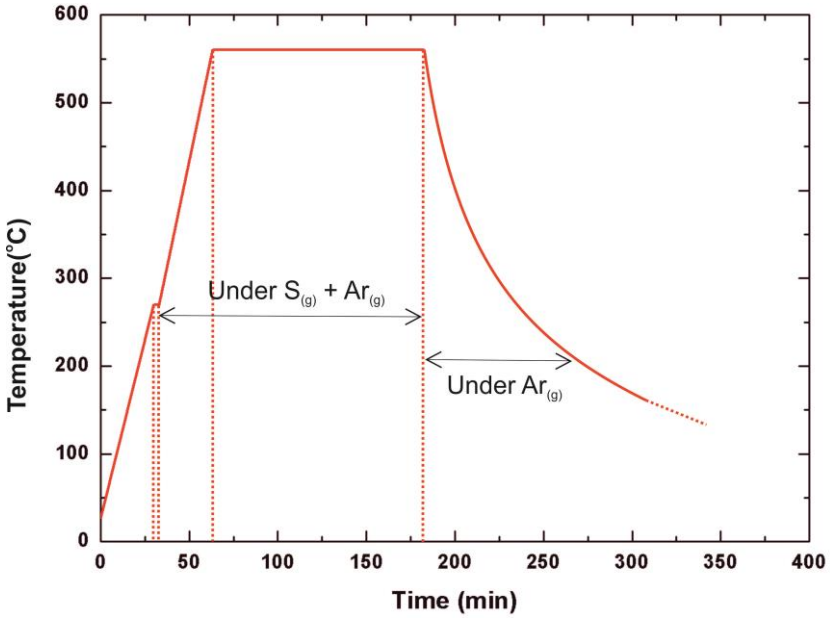

Figure 4.5. Sulfurization temperature and heating rate profile

4.4. Characterization of the Samples

4.4.1. Scanning Electron Microscopy (SEM)

To investigate the morphology of films SEM measurements are an important tool. It enables to see the crystal formation in a direct way. The operation principle is similar to optical microscope, but the instead of using light, electrons are used in SEM. Usage of smaller wavelength offers an advantage to see the material in an atomic level with a higher resolution. Since typical electron energies are in the range of 10-30 keV, smaller wavelengths than light are used.

4.4.2. Energy Dispersive X-Ray Spectroscopy (EDS)

EDS enables to investigate composition of the sample. Its operational principle is based on the bombardment of the sample with electrons and excitation of the bound electrons to leave the atomic shells. As a result these vacant shells are the filled up by electrons from outer shells. Since every element has a characteristic atomic structure, specific energies are produced and send through to detector to determine the content.

The growth morphology was investigated using a scanning electron microscope (SEM; FEI-QuantaFEG 250) which is equipped with Energy Dispersive Spectroscopy (EDS; Oxford X-act). EDS analysis of the samples gave us essential information about the stoichiometry of the films

4.4.3. X-Ray Diffraction (XRD) Analysis

Further analysis of the samples were done with XRD to identify secondary phase formations in our films. This technique is based on the diffraction of X-Ray waves by a crystal lattice. Principally, the wavelength of the wave should be in the range of the lattice constants, in order this effect to take place in the material.

The crystal structures of fabricated CZTS thin films were analysed by X-ray diffractometry (XRD). The XRD was operated in the Bragg-Brentano focusing geometry from 20^{o} to 80° on a Phillips X'Pert Pro X-Ray diffractometry, with Cu Kα radiation (λ=1.5406 Å) using a step size of 0.02° and a time step of 3 min. It is well known that, XRD analysis solely is not a competent technique for structural characterization of kesterite structure CZTS (JCPDS: 026-0575), due to the formation of analogue crystal structured second phases ZnS (JCPDS: 00-05-0566) and Cu_2SnS_3 (JCPDS: 00-027-0198). Therefore, Raman scattering analysis was also needed to obtain a complete and reliable analysis.

4.4.4. Raman Spectroscopy

Raman spectroscopy is an effective spectroscopic technique in the investigation of the material. Its operational principle relies on the inelastic scattering of monochromatic light. Generally, a laser source with the wavelength in the range of visible (390-700 nm), near infrared (700nm-1400nm) or near ultraviolet (300-400nm) is used. It relies on the light-matter interaction. Since elastic scattering takes place, the frequency of the monochromatic light changes after its interaction with the sample. The photons of the monochromatic light absorbed by the material and the reemitted with a shifted frequency. The comparison of these shifting with the original monochromatic frequency is

called Raman Shifts. These shifting provide information about the vibrational and rotational frequency transitions in molecules.

High-resolution Raman spectroscopy (Princeton Instruments, Acton SP2750 0.750 mm Imaging Triple Grating Monochrometer) with an excitation wavelength of 514.5 nm was used to obtain results that are more reliable.

4.4.5. X-ray Photoelectron Spectroscopy (XPS) Analysis

XPS is an analysis technique, which similar to EDS and XRF (X-Ray Fluorescence) techniques, enables to determine the composition besides; information about the chemical bonding of elements can be obtained since electron levels are influenced by bindings. This technique especially helpful in case of the sulfides and oxides investigations. Its operation principle is based on the photoelectric effect. Incoming X-Rays knock-out electrons from the sample. These samples are detected by a spectrometer then, gives chemical information about the impinged sample.

For this thesis, the compound elements and second phase formation were investigated using the XPS instrument. XPS measurements were performed with a monochromatized Mg K_α radiation source ($h\gamma = 1254$ eV) with a power of 200 W. The analyzer pass energy and the step size of energy were set to 30 eV and 0.1 eV for all elements, respectively. After measurements, all elements were referenced to C *1s* (284.6 eV). After Shirley background subtraction was added to XPS measurements, deconvolution process of the spectra was achieved with peak type of Gaussian-Lorentzian by using the PeakFit software.

4.4.6. Electrical and Optical Characterization

The CZTS material deposited on soda lime glass (SLG) substrate (SLG-CZTS) samples were investigated to reveal their electrical and optical characteristics. For this reason, four point probe measurements (Keithley 2182A nanovoltmeter, Keithley 7001 switch system, Keithley 220 programmable current source) and Hall effect measurements (Lakeshore 450 Gaussmeter and Phywe 06480.01 electromagnet) were performed to measure sheet resistance, resistivity, carrier concentration, and mobility of the CZTS

semiconducting compounds. A PerkinElmer Lambda 950 UV/VIS/NIR spectrometer was used for optical measurements. Optical absorption and transmission measurements were carried out for band-gap calculations. Film thicknesses were measured by Veeco DEKTAK 150 surface profilometer.

CHAPTER 5

RESULTS AND DISCUSSION

5.1. AFM Analysis of Metallic Foils

As-purchased metal foils have rough surface arising from the foil production process. In order to get rid of the textured surface of foils, polishing or coating a levelling layer is the necessary step in the case of foil substrate utilization (Kessler and Rudmann 2004). As mentioned earlier, to remove the oxidized layer and to decrease the surface roughness, the Ti and Mo foils were chemically etched before the sputtering process with diluted HF and HCl, respectively. Surface roughness of Ti and Mo foils were examined by AFM spectroscopy before and after etching. AFM images of untreated and etched Mo is shown in Figure 5.1. and 5.2, respectively. Figure 5.3 and 5.4 are AFM images of untreated and etched Ti foil, respectively. A decrement was observed in the surface roughness of Ti foil, however Mo foil surface got rougher after the etching process (Table 5.1). Due to the highly scratched surface of as-purchased Mo foil, scratch lines got deeper after etching with HCl.

Table 5.1. Surface roughness of Mo foil and Ti foil before and after etching

	Surface roughness (R_a, nm)	
	Before Etching	After etching
Mo Foil	24.905	26.131
Ti Foil	33.342	22.199

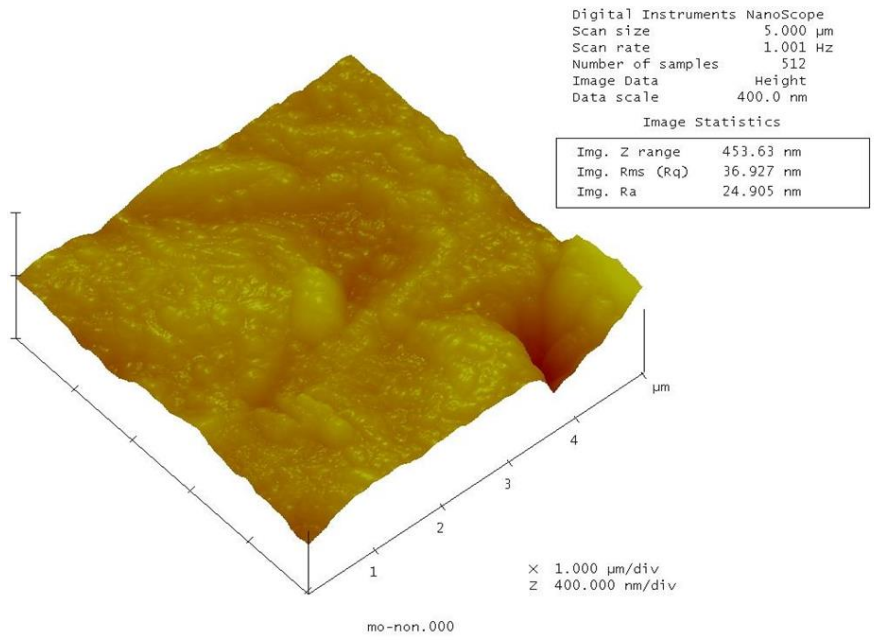

Figure 5.1. AFM images of untreated Mo foil

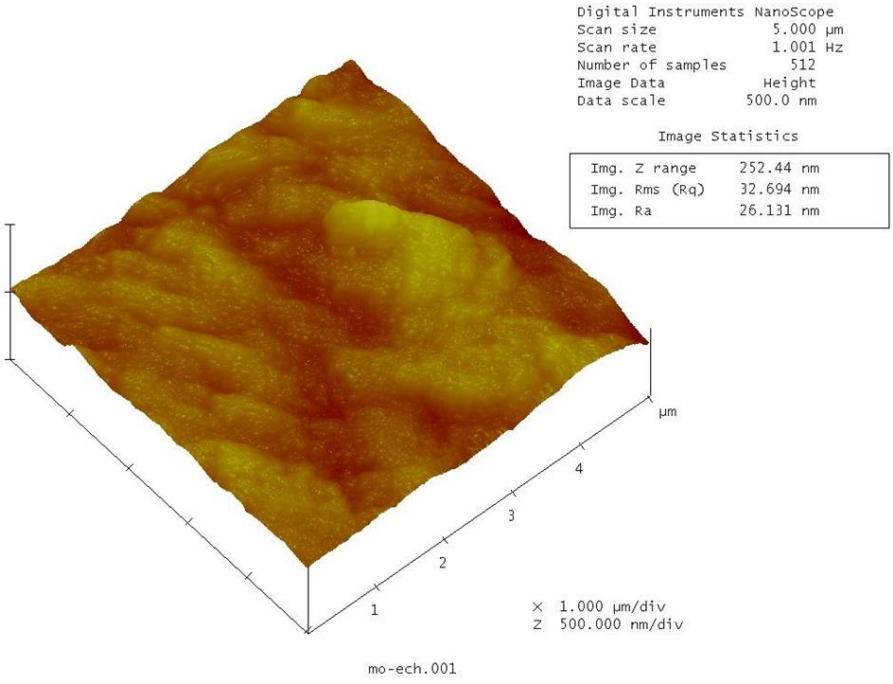

Figure 5.2. AFM images of etched Mo foil

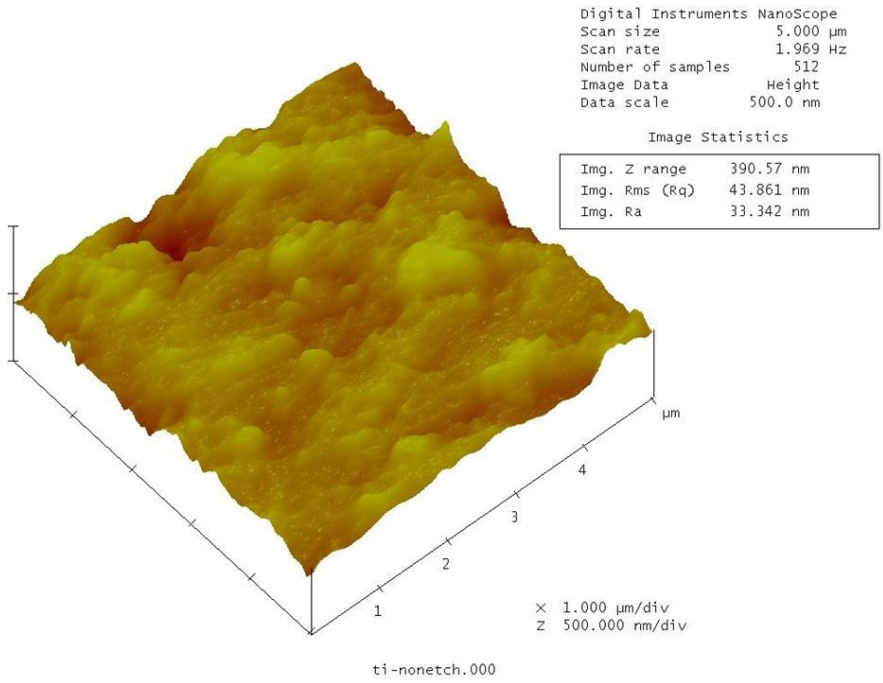

Figure 5.3. AFM images of untreated Ti foil

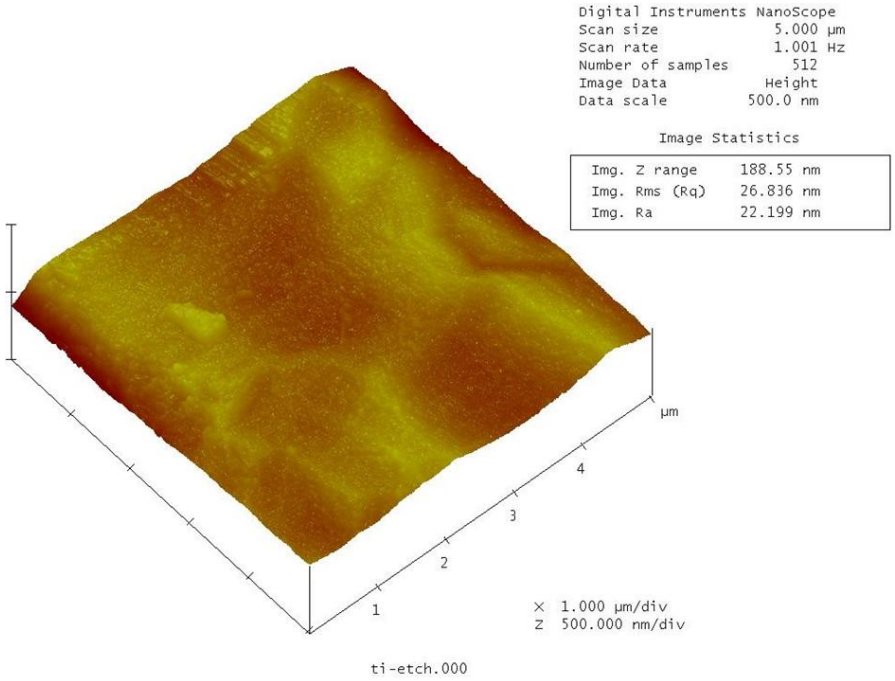

Figure 5.4. AFM images of etched Ti foil

The morphology of the absorber layer one of the most important parameter for the solar cell devices. A smooth substrate surface results in higher efficient solar cell. It has been reported in the literature that, substrate roughness has impact on the device efficiency due to the three reasons (Batchelor et al. 2004). It was asserted that, absorber

layer may grow with more nucleation centers, resulting in smaller grains and more defects on a rough substrate. Secondly, impurity diffusion may increase in the case for rough substrate, due to the imperfection in the coverage by the back contact. Lastly, rough surface topography creates shunt paths between the back and front contacts of the device.

5.2. Compositional and Morphological Analysis

The thicknesses of the Cu/Sn/Zn layers measured as 155, 360, and 175 nm, respectively via the profilometer. These thicknesses were targeted through molecular weight and density calculations for each element to get Cu_2ZnSnS_4. Since CZTS is a quaternary semiconducting compound, it exhibits a very complex structure. It requires systematic controlling of the conditions in both stages during the growth procedure of the CZTS layer. However, in the first stage of the process, to obtain metallic precursor, the sputtering method enables one to adjust the metallic content easily, just by changing the sputtering time and power. Additionally, sputtering method offers wide range of advantages like easy adaptation to large scale and reproducible manufacturing. In Figure 5.5 CZTS material deposited samples on Ti and Mo foils are illustrated.

Figure 5.5. Schematic representation of Ti and Mo foil substrate CZTS samples

For the purpose of availability to obtain CZTS absorber layers in a cost-effective way, metallic sputtering targets were used in contrast to those used in the other studies in the literature. The compositional analysis was done using EDS measurements and to study the growth morphology of the layers, SEM imaging technology was used. During the sulfurization process of the metallic precursor, sulfurization temperature and duration play a major role in the formation of the CZTS compound.

In the beginning of the research we examined the CZTS structure on SLG substrate. Sputtering powers and times were optimized according to the results of EDS

analysis. Structurally analyzed metallic precursors sulfurized by using different parameter (different temperatures and durations) till to get the optimum results deduced from Raman, XRD and EDS measurements. After calibration processes of both stages, CZTS structure obtained on 18 Ti foil , 16 Mo foil and 57 SLG substrates. Since we mostly focus on the electrical properties of CZTS material, the number of SLG-CZTS sample is quite higher than the foil samples.

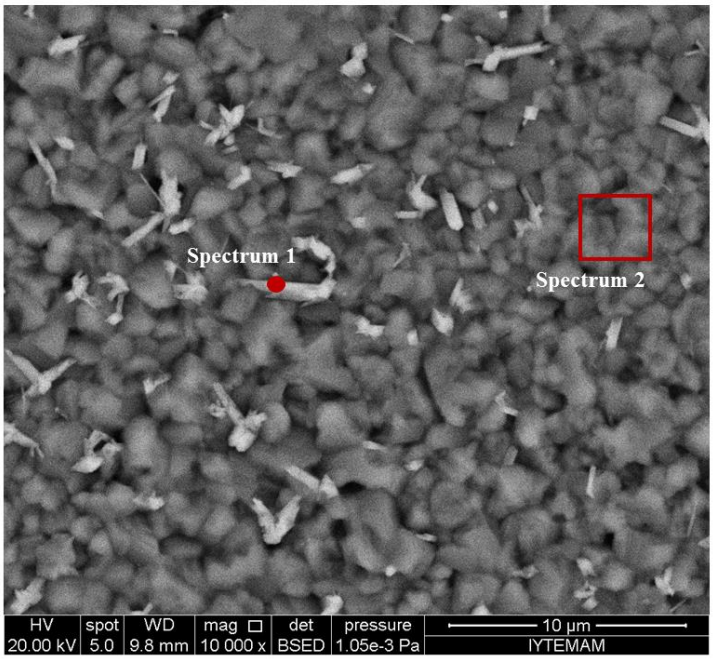

Figure 5.6. EDS analysis of CZTS-32 (substrate: SLG)

The SEM image in Figure 5.6 belongs to sample CZTS-32. This sample obtained on SLG substrate, without Mo back contact layer. The precursor state of this sample was deposited with the Zn/Sn/Cu layer ordering (from bottom to top). During the calibration process, it was found that to obtain the CZTS structure, high amount of sulfur is needed. Reaction of metal precursor with the sufficient amount of sulfur is crucially important to obtain CZTS alloy. The deposition times were adjusted to 5 min for Cu, Sn and Zn targets by tuning sputtering powers. It was aimed to achieve desired layer thicknesses in the same time span for all three targets. In this manner, we would be able to try the co-sputtering method in our future work.

Apart from bight needle shaped crystal formation (spectrum 1), dense and homogeny crystallization is dominant (Fig. 5.6). Distinct grains were not found, rather a nano-wire like bright color microstructures were observed. Table 5.2 lists the atomic

composition of SLG substrate sample, CZTS 32. The mention bright needle shaped crystal formation was encountered due to the Sn-rich composition of this sample. Overall the surface composition is denoted as spectrum 2 which shows sufficient sulfur content and slightly Zn-poor composition.

Table 5.2. The component ratio of the sulfurized sample CZTS-32

	Cu (Atomic %)	**Zn (Atomic %)**	**Sn (Atomic %)**	**S (Atomic %)**
Spectrum 1	16.63	7.29	34.71	41.36
Spectrum 2	24.74	11.57	12.47	51.21

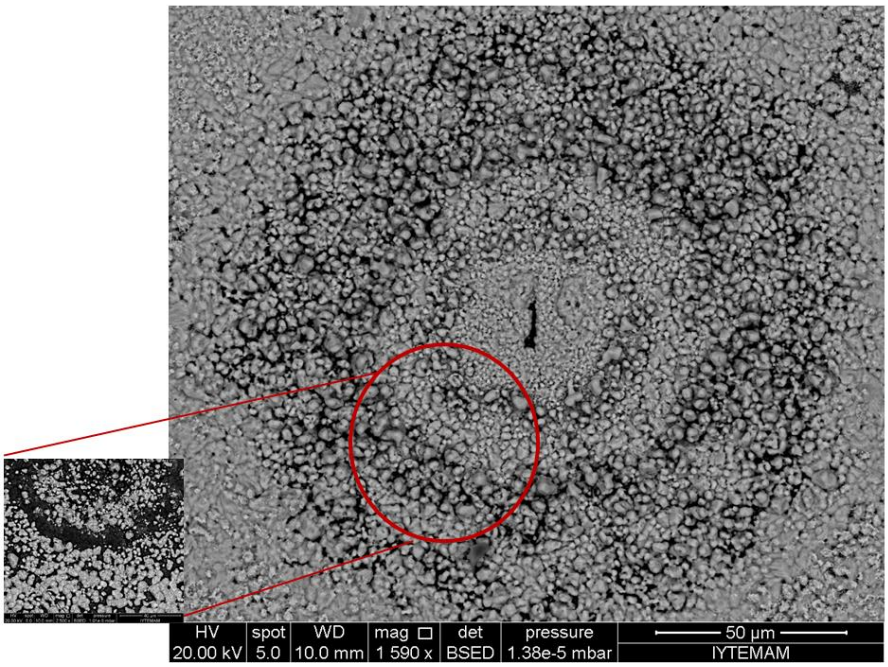

Figure 5.7. SEM image of CZTS-36 (substrate: ceramics, Ti back contact)

In Figure 5.7, SEM image of CZTS-36 is shown. The substrate of this sample is Ti thin film coated Sinterflex ceramics. Distinct grains were observed. The rounded shaped crystal formation is consistent with the the formation of Sn-based second pahase formations (Scragg 2010). This crystal formation is shown in higher magnification is Fig. 5.8. It is seen that, due to the oxidation of the Ti thin film layer, adhesion of the metallic layer was poor on that surface. Spectrum1 reveals poor adhesion for this sample. Table 5.3 lists the atomic composition of sample that obtain via EDS analysis.

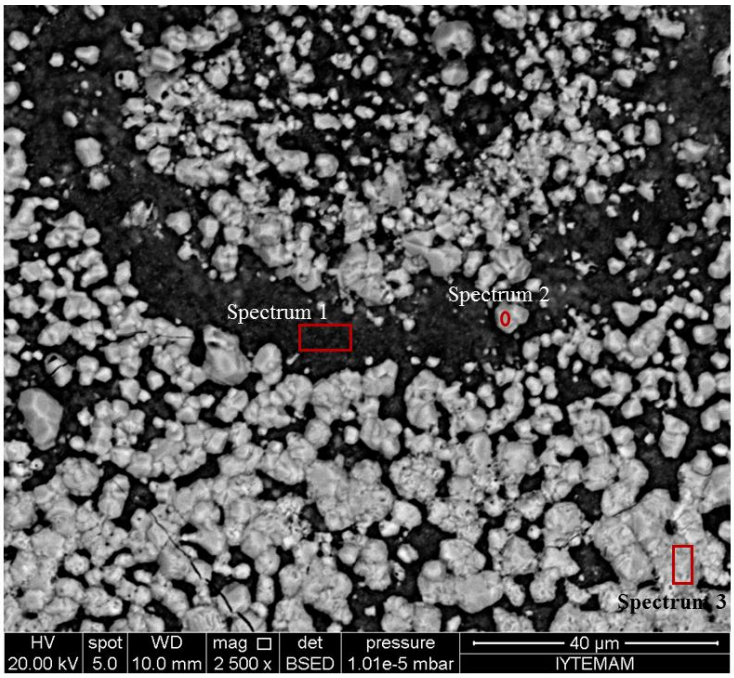

Figure 5.8. SEM image of CZTS-36 (Ti/ceramics)

Table 5.3. The component ratio of the sulfurized sample CZTS-36 (Ti/ceramics)

	Cu (Atomic %)	**Zn (Atomic %)**	**Sn (Atomic %)**	**S (Atomic %)**	**Ti (Atomic %)**
Spectrum 1	2.20	1.46	2.01	5.33	89.01
Spectrum 2	23.52	11.25	13.33	51.90	-
Spectrum 3	19.16	8.48	20.71	51.66	-

As can be seen in Table 5.3, spectrum 1 is highly Ti rich, means deposition of metallic layer was unsuccessful. To investigate the crystal formation in both region, distinct crystals were determined during the EDS analysis and named as spectrum 2 and spectrum 3. EDS analysis of spectrum 2 revealed the slightly Sn-rich composition while spectrum 3 belongs to highly Sn-rich crystals.

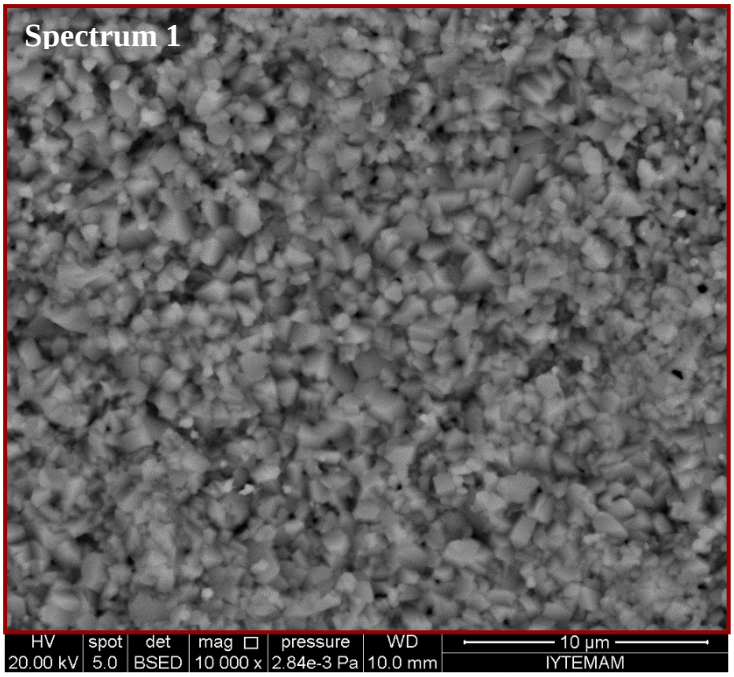

Figure 5.9. SEM image of CZTS-58 (substrate: Ti foil)

As shown in Table 5.4 the atomic compositions of the sample CZTS-58 is poor in Zn, rich in Sn contents. By matching Table 5.4 and Figure 5.9 it can be seen that, spectrum 1 in the CZTS, occupy larger areas and are distributed more uniformly within the samples, and have better compositions than other previously obtained samples. It composed of densely packed grains. The CZTS-58 sample was deposited on chemically etched Ti foil with the Zn/Sn/Cu layer ordering.

Table 5.4. The component ratio of the sulfurized sample CZTS-58

	Cu (Atomic %)	**Zn (Atomic %)**	**Sn (Atomic %)**	**S (Atomic %)**
Spectrum 1	22.74	11.33	13.81	52.12

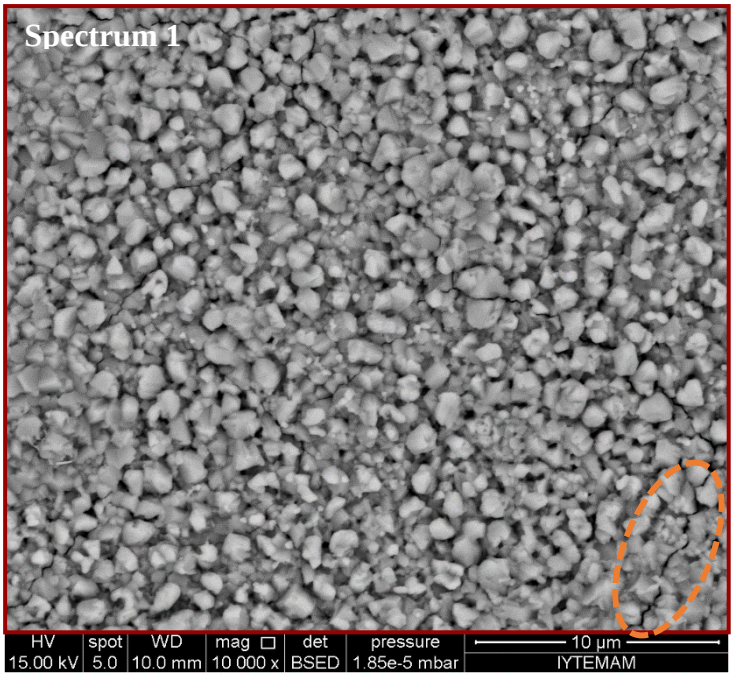

Figure 5.10. EDS analysis of CZTS-63 (substrate: Mo foil)

The SEM images of CZTS-63 is shown in Figure 5.10. The surface SEM image of the CZTS-63 indicates that the film exhibits a rough surface containing micron-sized particles. The crack formation on the layer is noticeably evident, and one of the cracks is highlighted with a dashed circle. It is assumed that low thermal expansion of Mo (4.8 x 10^{-6} K^{-1}) is responsible for this deformation. In contrast, crack formation or delamination were not observed in the samples on Ti foil substrate.

The Ti-CZTS and Mo-CZTS samples were obtained from a single sputtering run with a double-faced sample holder apparatus. Then, the metallic precursors were produced identically. Additionally, the same sulfurization parameters were used to be able to investigate the substrate effect on the CZTS structure formation. Table 5.5 lists the atomic weight percentages of the constituent elements of CZTS-63.

Table 5.5. The component ratio of the sulfurized sample CZTS-63

	Cu (Atomic %)	**Zn (Atomic %)**	**Sn (Atomic %)**	**S (Atomic %)**
Spectrum 1	22.78	10.71	13.49	53.02

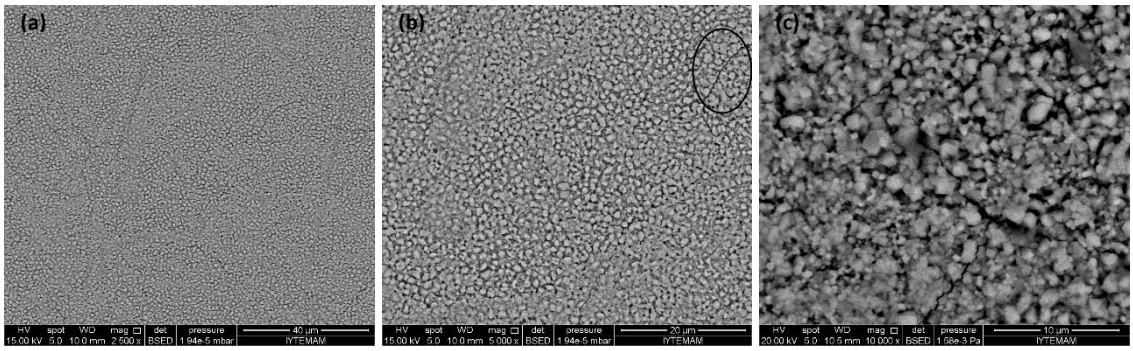

Figure 5.11. SEM images of CZTS on Mo foil substrate at (a)2.50 kX, (b)5.00 kX, and (c)10.00 kX magnification

In Figure 5.11 the crack formation of Mo-CZTS sample is shown more clear in SEM images with three different magnifications.

5.3. Structural Analyses

5.3.1. XRD Analysis

To get insights of the crystal formation of our samples, beyond compositional analysis XRD analysis was done to reveal information about the crystal structure and existing phases. However, the problem with the XRD analysis of CZTS structure is that, peaks often overlap. Since the peaks of CZTS, Cu_2SnS_3 (CTS) and ZnS-which all have the sphalerite structure- overlap, this makes nearly impossible to identify the CZTS structure clearly. Fortunately, CZTS and CTS have some small extra peaks which ZnS phase do not exhibits. On the other hand, ZnS does not have any distinctive peak. That means, ZnS can never be excluded from possibly present CZTS and/or CTS phases.

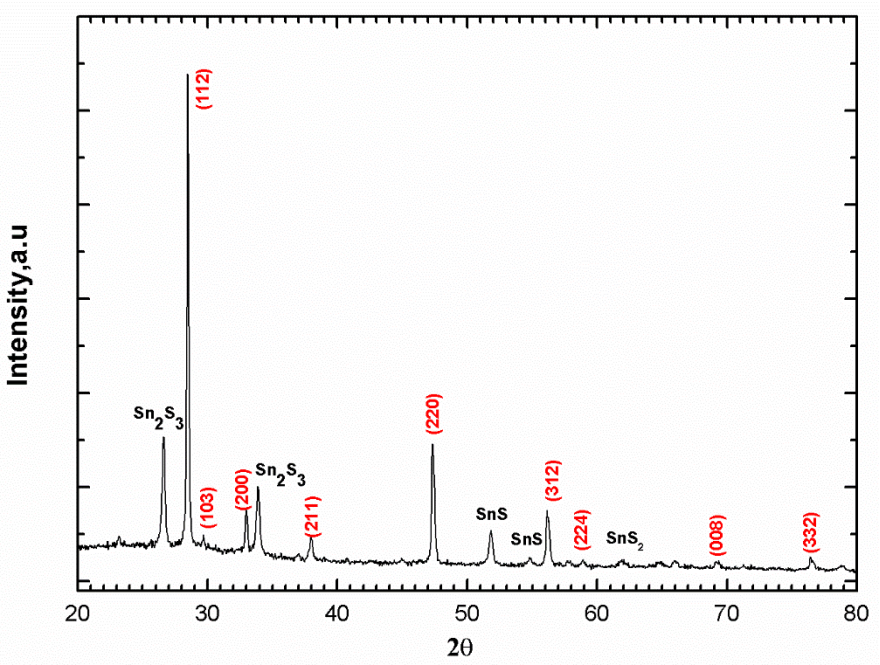

Figure 5.12. XRD Diffractogram of CZTS-32 (substrate: SLG)

The XRD analysis of the sample CZTS-32 confirmed that it has the well-matched diffraction peaks that of CZTS semiconductor material reported in JCPDS (Joint Committee on Power Diffraction Standards) 26-575 (Figure 5.12) . This data base was used during the XRD characterization of the samples. In Figure 5.12, the sharp peaks of the film (red) at 2θ = 28.56°, 29.6°, 32.99°, 47.3°, 56.2°, 58.97°,69. 30° and 76.44° are in good agreement with the diffraction of the (112), (103), (200), (220), (312), (224), (008) and (332) planes of CZTS (JCPDS no. 26-0575), respectively, which clearly indicates the perfect kesterite structure of CZTS. Apart from the peaks assigned to CZTS structure, Sn-rich composition leads to Sn-based binary secondary phase formations. These peaks were assigned by the X-Pert HighScore Plus where SearchMatch property embedded in it. Since the simultaneously formed ZnS (JCPDS: 00-05-0566) and Cu_2SnS_3 (JCPDS:00-027-0198) secondary phases have very similar crystal structures with kesterite CZTS, XRD analysis is not a sufficient analysis technique to detect kesterite CZTS structure (JCPDS: 026-0575) (Fig. 5.13). To obtain more reliable result XRD analysis should be compared with Raman spectroscopy analysis.

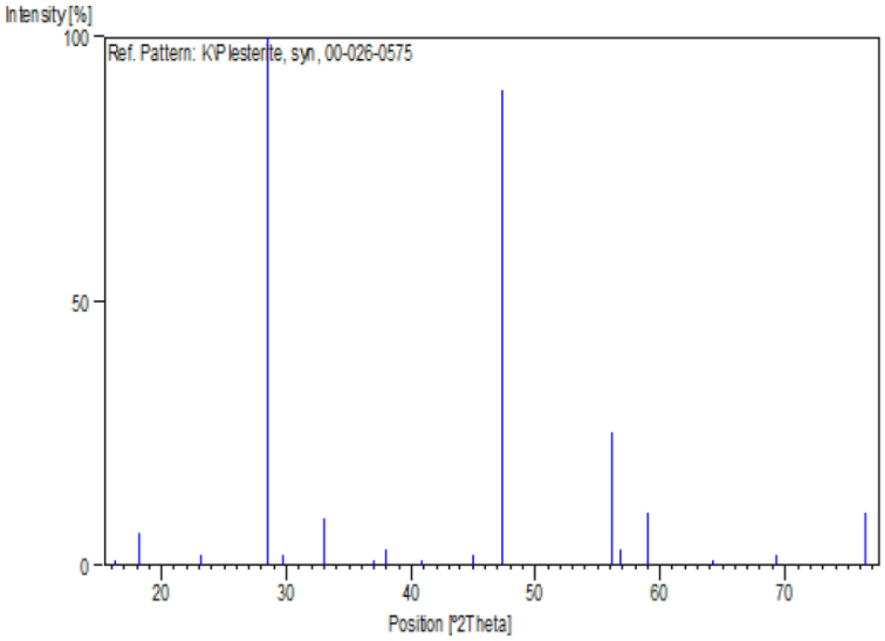

Figure 5.13. Reference XRD pattern of Kesterite CZTS
(Source: JCPDS: 026-0575)

The Figure 5.14 belongs to XRD pattern of the sample CZTS-36 that is deposited on Ti coated ceramic substrate. To be able to exclude the diffraction peaks from ceramic substrate and Ti coating on the substrate, all three state of the samples XRD pattern were placed in this figure. In Figure 5.14(a), a preferential orientation (112) was observed. The diffraction peaks from the (112), (220), (312), (224) and (332) planes, which indicate the formation of kesterite CZTS, are clearly shown for all three samples (JCPDS card: 26-0575). Additionally, small peaks at 37.10^{o} (202), 38.00^{o} (211) and 44.09^{o} (105) and the (213) peak suggest the formation of the CZTS structure (Schorr 2007). However, as mentioned earlier, because of the similarity of the lattice parameters in the ternary and binary phases that may arise during the growth of the CZTS layer, XRD analysis alone cannot confirm the existence of the CZTS structure.

Figure 5.14(b) that is belong to Ti coated ceramic, does not show any intense Ti signals. It can be deduced that, Ti coating on ceramic was not well crystallized.

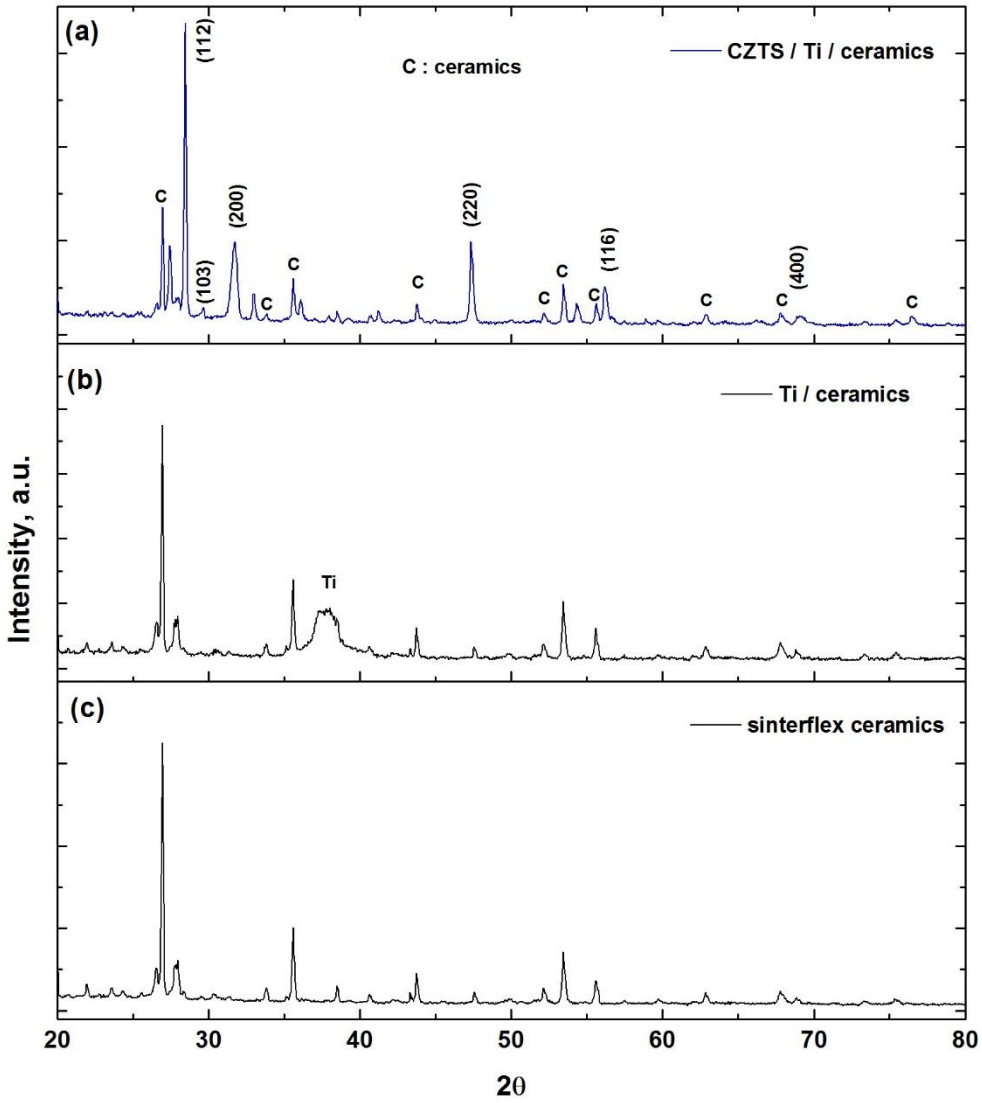

Figure 5.14. XRD pattern of (a) CZTS/Ti/ceramics, (b) Ti/ceramics, (c) ceramics

The Figure 5.15 is the XRD pattern of CZTS-58 that is obtained on Ti foil substrate. Besides, the preferential (112) peak and other CZTS structure related peaks, this sample shows the existence of a crystalline SnS phase. This is an expected result, since the EDS measurements revealed Sn-rich composition (Cu/Sn=1.6, while 2 would be stoichiometric).

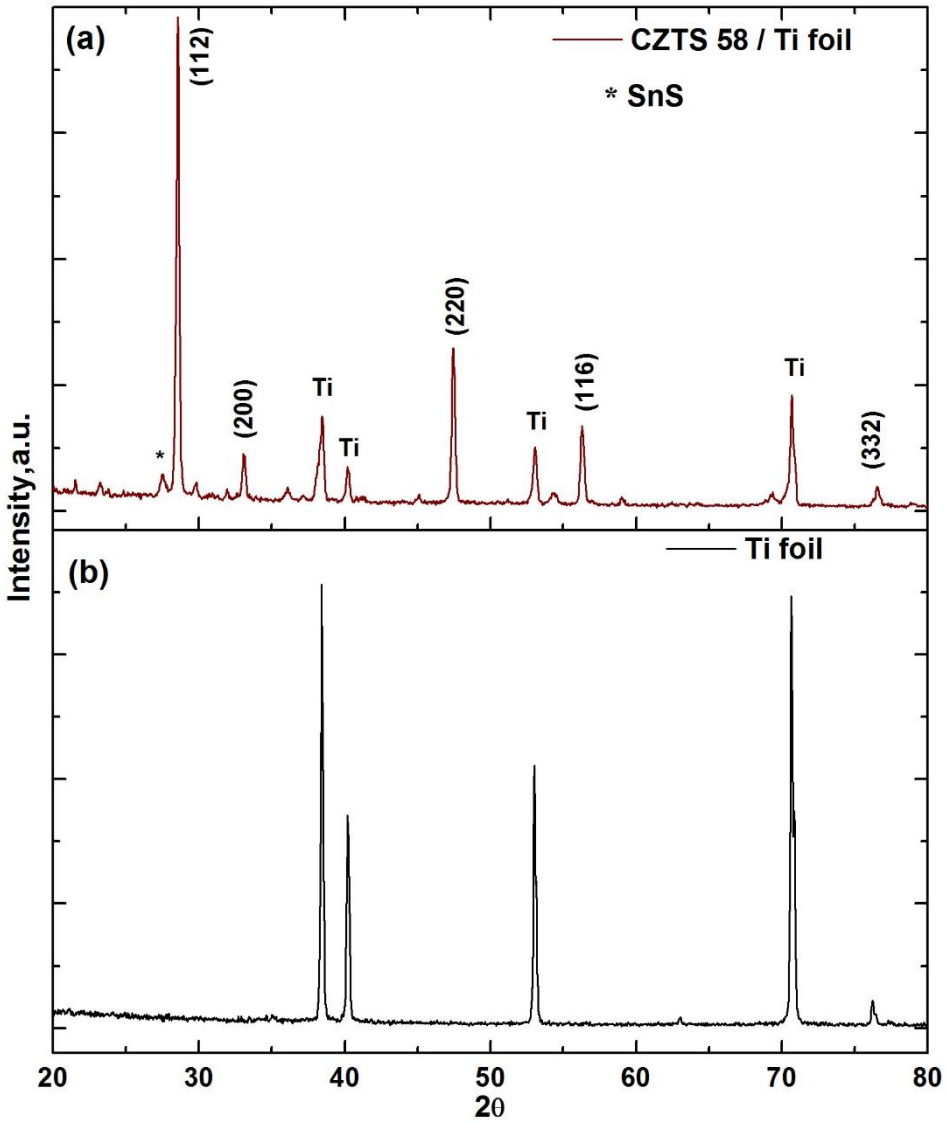

Figure 5.15. XRD pattern of (a) CZTS-58, (b) Ti foil

XRD pattern of CZTS-63 that is deposited on Mo foil is shown in Figure 5.16. It does not show any trace of secondary phases. However, the absence of an XRD peak does not have to mean absence of the secondary phase, since it could be present in amorphous phase.

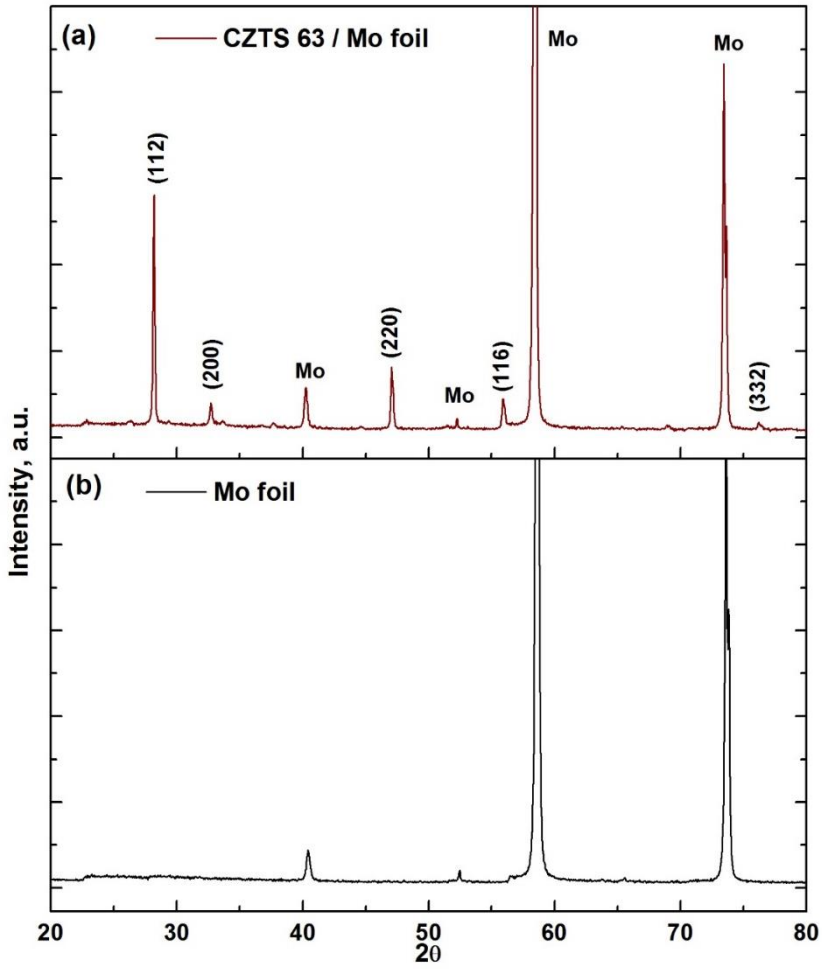

Figure 5.16. XRD pattern of (a) CZTS-63, (b) Mo foil

The XRD peaks were often present at different intensities. In principle, the intensity should be only compared with the pattern of the related structure in a data base. Figure 5.17 shows the relative intensities of main peaks with respect to (112) preferential plane of Ti-CZTS, Mo-CZTS and reference CZTS obtained from database. The intensities for each diffraction peaks in the experimental diffractograms were compared with the equivalent diffractograms for the powder reference, JCPDS 026-057. The experimental conditions for Ti-CZTS and Mo-CZTS diffractograms were kept the same.

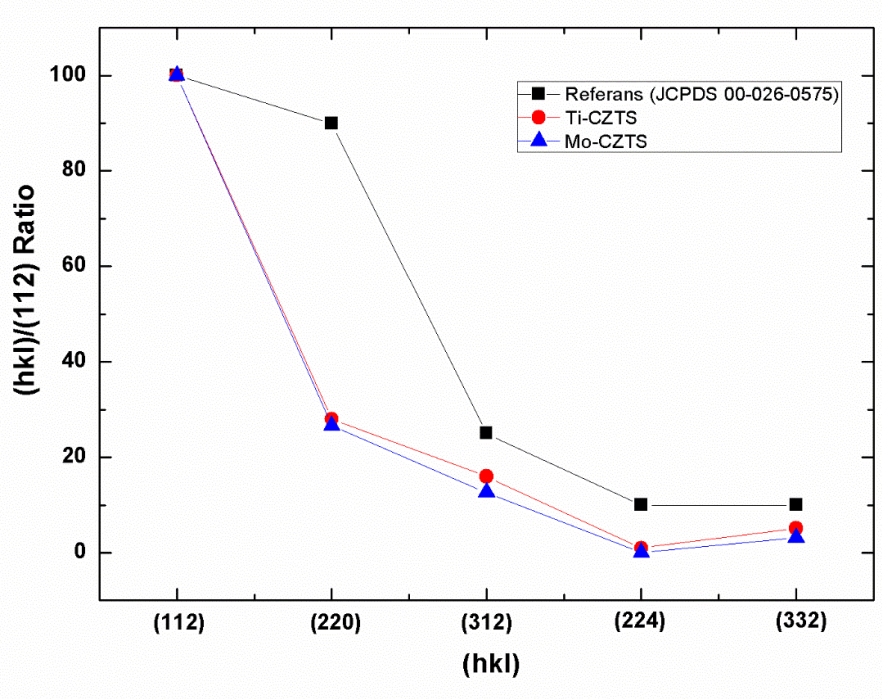

Figure 5.17. (hkl)/(112) preferential plane ratio of CZTS structure deposited on two different foil substrates

5.3.2. Raman Spectroscopy Analysis

The Raman spectra of CZTS 32 is shown in Fig.5.18. It reveals Sn-based second phase formation in this sample, which is a coherent outcome with the XRD and EDS analyses. The intensities of the Raman peaks of these Sn based secondary phases are considerably small compare to CZTS main Raman peak at 336cm^{-1}.

Figure 5.19 shows the Raman scattering analysis of CZTS-36. The most intense Raman mode is at 338 cm^{-1}, which is attributed to the vibration of S atoms having A_1 symmetry of the kesterite structure CZTS material (Mitzi et al. 2011a)(Lin et al. 2012)(Altosaar et al. 2008). The other peaks located at 288, 252 and 374 cm^{-1} are the characteristic vibration modes of CZTS material (Mitzi et al. 2011b). In addition to characteristic CZTS peaks, the peaks at 445 and 610 cm^{-1} revealed the existence of the rutile TiO_2 phases (Krishnamurti 1962).

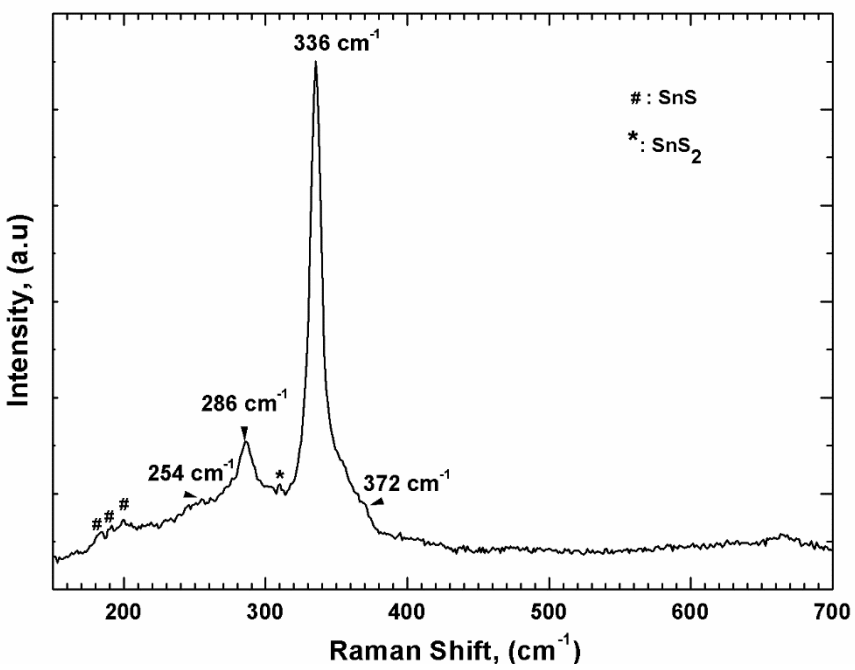

Figure 5.18. Raman Spectra of CZTS-32 (substrate: SLG)

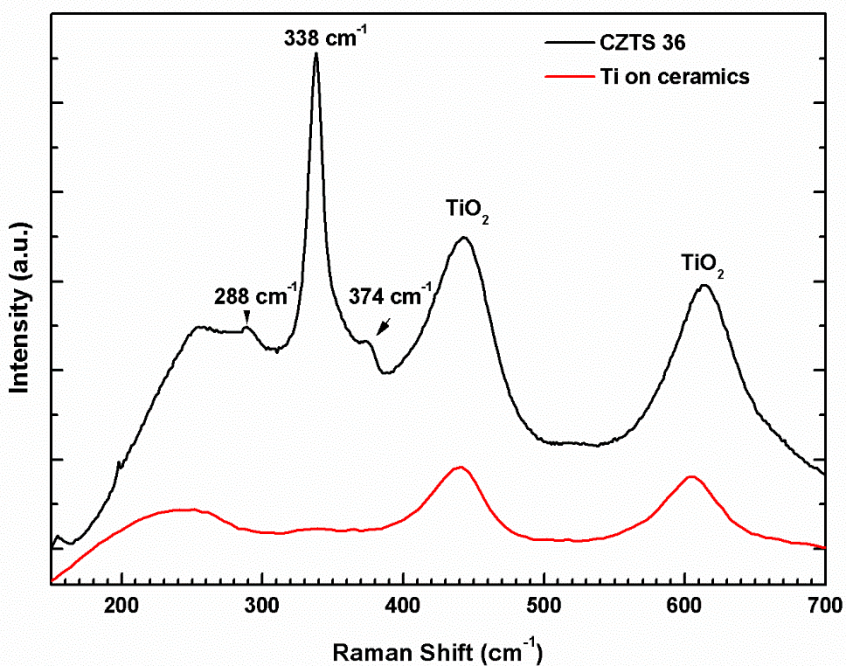

Figure 5.19. Raman Spectra of CZTS-36 (substrate: Ti thin film coated ceramics)

The Figure 5.20 belongs to CZTS-58 and it proves the existence of kesterite structure CZTS material on Ti foil substrate. To analyze the presence of possible secondary phases with Raman spectra, the particular Raman modes of these phases must be known. It was reported that there is a single Raman peak for SnS_2 at 314 cm^{-1}, while SnS has three peaks at 160 cm^{-1}, 190 cm^{-1} and 219 cm^{-1} (Cheng et al. 2011) . $Cu_{2-x}S$ has

a strong peak at 475 cm^{-1} and a weaker peak at 264 cm^{-1} (Fernandes, Salomé, and Cunha 2010)., In Figure 5.20, the small peaks that are located at 190 and 220 cm^{-1} belongs to SnS phase. This is a coherent deduction, since both EDS and XRD analysis revealed the existence of Sn based secondary phase formation. These are an excellent match to tin monosulfide, SnS (Price et al. 1999).

The Raman spectra belong to CZTS-63 (Fig.5.21) did not show any trace of secondary phases related with CZTS. However, the peaks located at 388 and 410 cm^{-1} revealed the formation of MoS_2 (Sandoval et al. 1991).

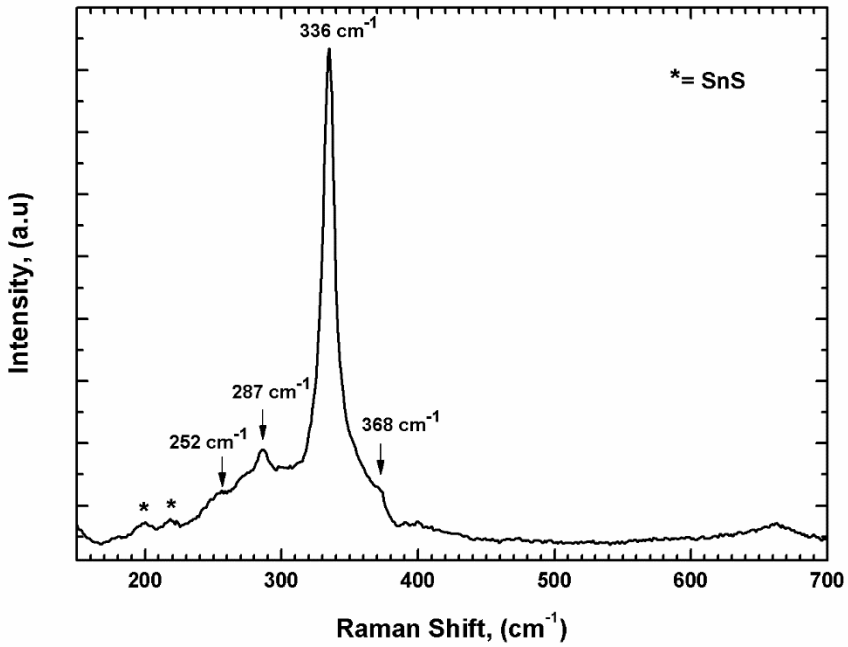

Figure 5.20. Raman Spectra of CZTS-58 (substrate: Ti foil)

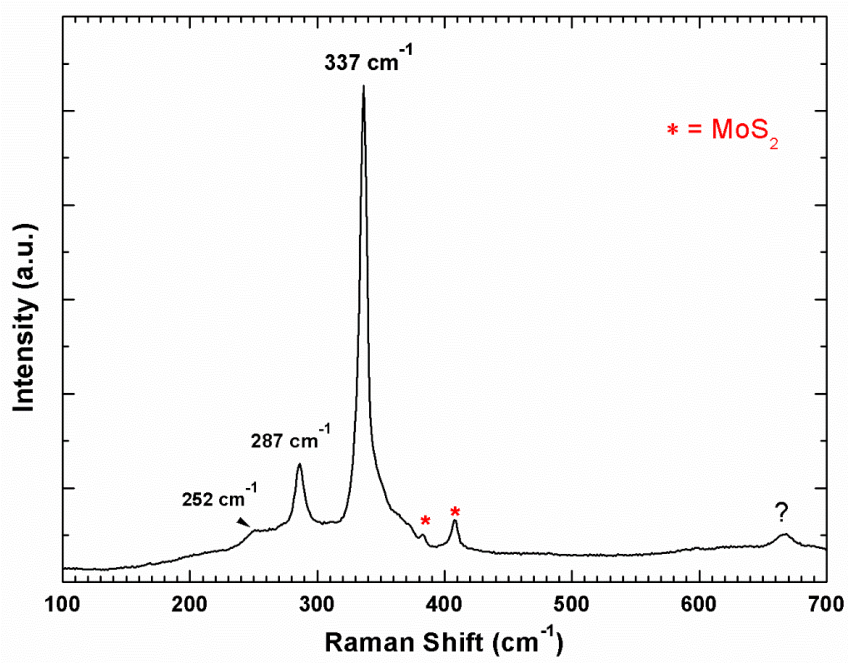

Figure 5.21. Raman spectra of CZTS-63 (substrate: Mo foil)

5.3.3. Effects of Chemical Etching

CZTS layers on untreated and etched Mo and Ti foils were analyzed and compared with each other to ensure the removal of the unrequired oxidized layer. The removal of Ti-oxide layer can be clearly seen in the XRD (Fig. 5.22) and Raman analysis (Fig. 5.23). The diffraction peaks of rutile and anatase TiO_2 are more intensive for untreated Ti-CZTS than those of etched samples. Coherently, Raman analysis of untreated Ti-CZTS revealed the existence of the rutile phases with the peaks located at 445 and 610 cm^{-1} (Krishnamurti, 1962). The peaks at 337, 288, 252 and 372 cm-1 are the characteristic vibration modes of CZTS material (Mitzi et al. 2011b).

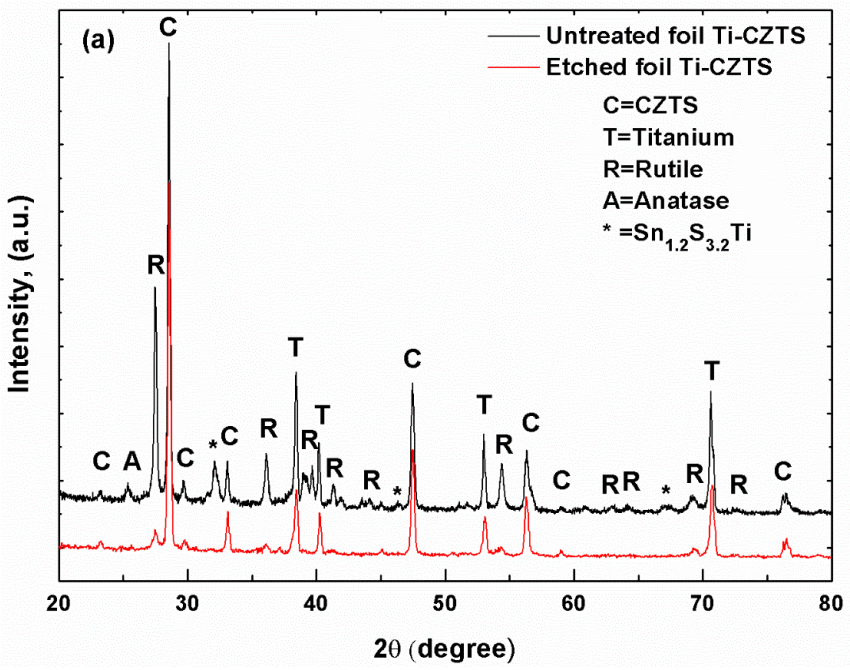

Figure 5.22. XRD diffractograms of CZTS material on untreated (black) and etched (red) Ti foil substrates

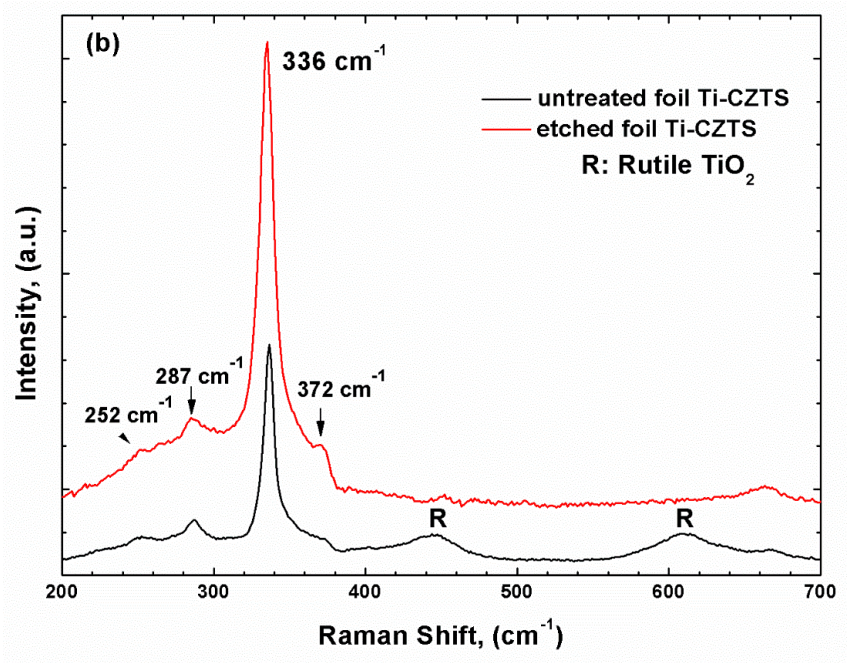

Figure 5.23. Raman Spectroscopy of CZTS material on untreated (black) and etched (red) Ti foil substrates

In the same way, we compared the XRD plots of CZTS material deposited on untreated and etched Mo foil substrates (Figure 5.24). Even though there is not any prominent oxide peaks, the relative intensity of preferential plane (112) of CZTS structure is considerably higher than that of non-etched Mo-CZTS sample. In Figure 5.25,

there is not any traces for the oxidized layer in the Raman spectroscopy for untreated Mo foil. Additionally, the characteristic Raman peak at 336 cm^{-1} is more intensive for nontreated than that of etched Mo-CZTS sample. Even though surface roughness was increased after etching, Raman and XRD analysis revealed better outcomes. Therefore, we preferred to use etched Mo-foils.

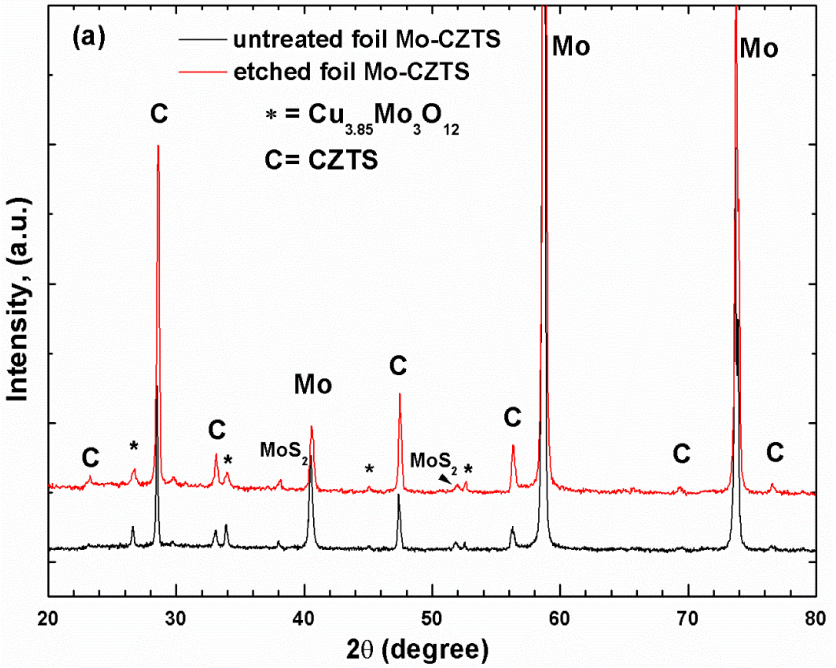

Figure 5.24. a) XRD diffractograms of CZTS material on untreated (black) and etched (red) Mo foil substrates

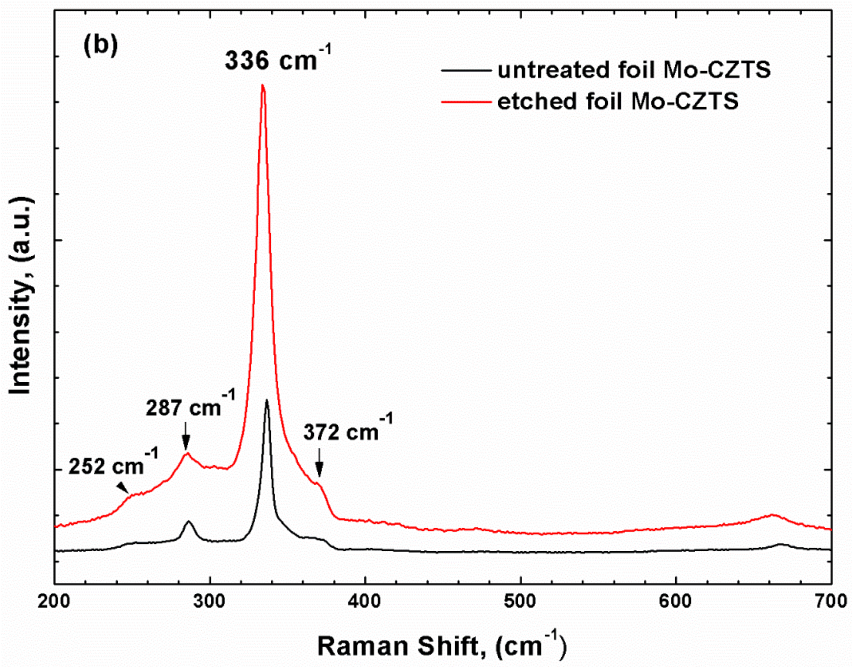

Figure 5.25. Raman Spectroscopy of of CZTS material on untreated (black) and etched (red) Mo foil substrates

5.4. Chemical Analysis

The compound elements, secondary phase formations and surface atomic concentrations of CZTS films on Ti and Mo foil were investigated using XPS. Figure 5.26 shows the XPS spectrum of CZTS 58 (Ti foil substrate sample) and CZTS 63 (Mo foil substrate). The surface spectrum of the CZTS films show a peak of C *1s* with negligible intensity, indicating that the surfaces of the films are clean enough after short air exposure. The presence of Cu, Zn, Sn and S elements were identfied from the survey spectra of the CZTS films. In addition to the survey scan, to determine.

The XPS measurement for Zn *2p* is given in Fig. 5.26b. Since Zn $2p_{3/2}$ and $2p_{1/2}$ peaks with a peak splitting of 23.1 eV for Mo-CZTS and 23 eV for Ti-CZTS close to the standard splitting value of 22.9 eV, they confirm the bivalent character, Zn II (Jiang 2011)(Mali et al. 2012). Edler *et al.* intentionally fabricated ZnS to determine the peak positions of Zn atoms in Zn sulfide and to compare with Zn atoms in CZTS. Their investigations revealed that the binding energy of the Zn *2p* electrons in Zn sulfide appears at lower binding energy sides than that of Zn atoms in CZTS (Edler et al. 2012). With reference to this, for both films, it was not observed the formation of a secondary ZnS phase.

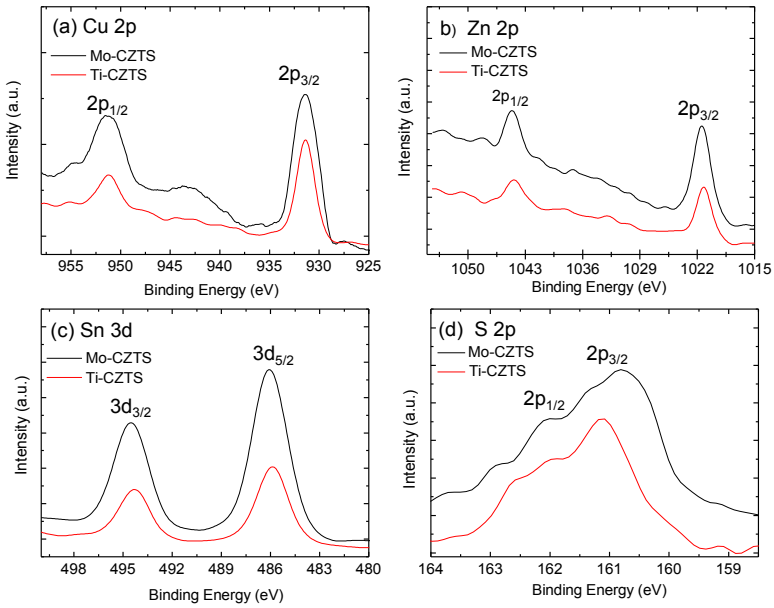

Figure 5.26. XPS spectrum of the CZTS thin films: core-level spectra of (a) Cu 2p, (b) Zn 2p, (c) Sn 3d, and (d) S 2p (subatrate: Mo foil (black line), Ti foil (red line)

SLG-CZTS, refers to a sample which was grown on a soda lime glass substrate. SLG substrate was used to measure the electrical and optical properties of the compound semiconductor thin film CZTS. It is well known that, important optical and electrical properties of the deposited thin film are directly dependent on the physical parameters of the magnetic sputtering process. The optical band gap energy of the film was determined by transmittance and reflectance measurements. Fig. 5.27 shows the plot of $(\alpha h\gamma)^2$ vs. photon energy to determine optical energy band gap of SLG-CZTS thin film.

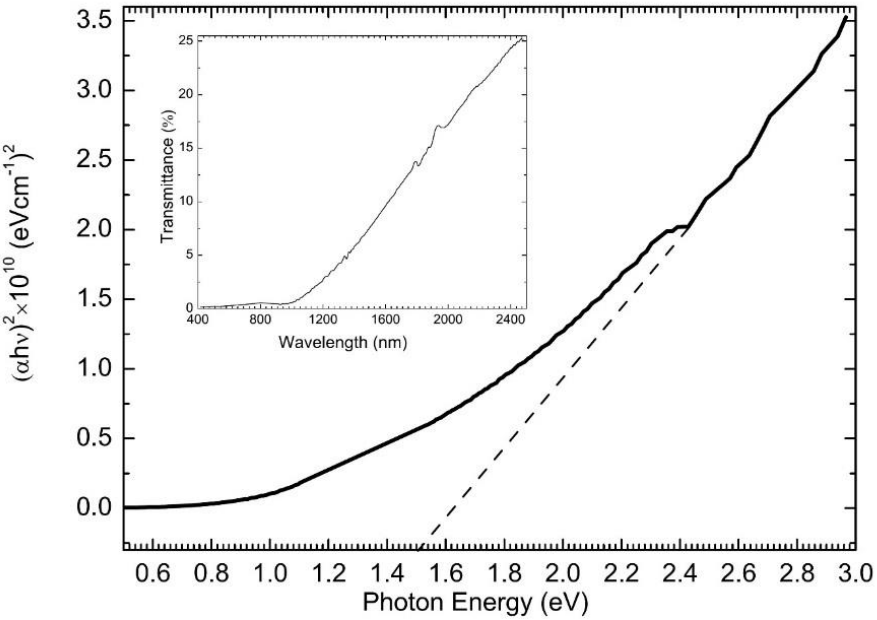

Figure 5.27. The $(\alpha h\nu)^2$ vs. photon energy plot for optical band gap determination; inset graph: the transmittance spectrum of a CZTS thin film on SLG

From Fig. 5.27, the intercept of the straight line on the photon energy axis gives the optical band gap energy value, E_g, of 1.52 eV, which is consistent with the optical band gap energy of the bulk form of CZTS in the range of 1.4 -1.5 eV (Jimbo et al. 2007). It is well known that the existence of secondary phases with band gap energies higher than that of the CZTS thin film (without secondary phases) have an impact on the band gap energy of the CZTS thin film (Parenteau and Carlone 1990). For SLG-CZTS, the only secondary phase observed was tin sulfide (SnS). The acceptable Eg value of SLG-CZTS is most likely due to the low band gap energy of SnS, which has a direct band gap in the range of 1.3 -1.42 eV and an indirect band gap of 1.1 eV (Tanusevski and Poelman 2003).

$Cu_2ZnSnSe_4$ is analogous to Cu_2ZnSnS_4 in terms of the Cu/Zn+Sn chemical composition. Babu et al. found that the band gap energy of CZTSe shift to higher energy levels as the Cu/Zn+Sn composition decreases (Babu et al 2010). It was predicted that this change in the band gap due to p-d hybridization between Cu d-levels and Se p-levels (Tanaka et al. 2011). In our work, the chemical composition ratio of Cu/Zn+Sn is lower than the stoichiometry. Therefore, the band gap energy of CZTS shifts to higher level due to changing in the p-d hybridization between Cu d-levels and S p-levels. Also the band gap might be shifted due to formation of high band gap material, SnS2 (2.2 eV), during the CZTS synthesis.

5.6. Electrical Characterization

The SLG-CZTS sample was cut into small rectangular shapes using a diamond cutter. Film sheet resistance was measured between thin copper electrical contacts that were adhered to the film using silver epoxy (Fig. 5.28(a)). Sheet resistance and resistivity of the film at room temperature were measured as 244 Ω/□ and 0.024 ohm.cm, respectively. (Patel, Mukhopadhyay, and Ray 2012) obtained similar results for CZTS prepared by a spray pyrolysis technique.

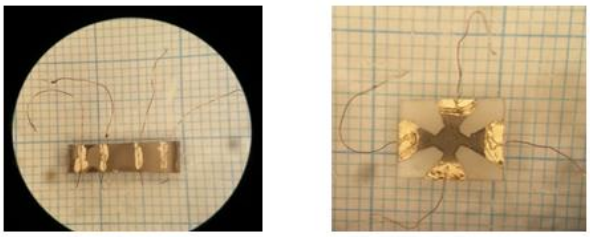

Figure 5.28. Electrically contacted CZTS 32 for (a) four probe point analysis, (b) Hall effect measurement with Van der Paow method

Van der Pauw and Hall effect methods were used to determine the electrical resistivity and the majority charge carriers, respectively (Figure 5.28(b)). The type of conductivity was determined as p-type via Hall effect measurements. The carrier concentration was found as $6.8x10^{20}$ cm^{-3}, and the mobility of charge carriers was 0.40 cm^2/Vs. However, the prevalent surface inhomogeneity problem with CZTS layer

makes the interpretation of the electrical measurements rather complicated, the values of the carrier density were found to be in agreement with previous studies (Rajeshmon et al. 2011).

CHAPTER 6

CONCLUSION

The choice of substrate is a very important issue for polycrystalline thin film photovoltaics, since the high temperature sintering is required to grow films homogenously. The substrate should behave chemically inert to not react with the chalcogen S, while being vacuum compatible.

As seen in the SEM images of Mo-CZTS samples, coefficient of thermal expansion has crucial effect in order not to encounter cracks, delamination, and poor adhesion. The Ti foils with (8.4-8.6) x 10^{-6} K^{-1} thermal expansion coefficient enable us grow uniform CZTS films without any degradation., while Furthermore, beside some impurity, which was predicted to be responsible for the peak at 460 cm^{-1} observed in Raman spectra, nearly pure CZTS layers were grown onto both metallic foils. Oppositely, there were not any impurity peaks detected for Ti foil. This conclusion is consistent with XRD patterns of the samples. This conclusion is clearly consistent with the XRD patterns of the samples.

In the electrical characterization of SLG-CZTS, it was concluded that the resistivity of the samples is small; therefore, the prepared samples can be used as an absorber layer in the fabrication of thin film solar cells.

Formation of cracks decreases the performance of the device since it creates shunt paths between the back and front contacts of the device. Micro-cracks are also inactive cell domains and thus, they reduce the active cell area. Therefore, back contact with nearly equal thermal expansion coefficient of absorber layer is preferable to reduce the possibility of crack formation. Additionally, since surface roughness of the metal substrate causes leakage current and pinholes, surface smoothness of a metallic substrate is another important factor to achieve high efficient flexible solar cells, and smooth surface may ensure easier and more homogenous active layer deposition.

Crack formation was detected on Mo-CZTS due to the mismatch between the thermal expansion coefficients of the Mo and CZTS. Since uniform CZTS films without any degradations were grown on Ti foil with, it was concluded that the Ti was the preferred foil with regard to its costs and physical properties in this study.

REFERENCES

Altosaar, M., J. Raudoja, K. Timmo, M. Danilson, M. Grossberg, J. Krustok,E. Mellikov. 2008. "$Cu_2Zn_{1-X}Cd_XSn(Se_{1-y}S_y)_4$ Solid Solutions as Absorber Materials for Solar Cells." *Physica Status Solidi (a)* 205 (1): 167–70

Araki H., A. Mikaduki, Y.Kubo, T. Sato, K. Jimbo, W. S. Maw, H. Katagiri, M. Yamazaki, K. Oishi, A. Takeuchi. 2008. "Preparation of Cu_2ZnSnS_4 thin films by sulfurization of stacked metallic layers", *Thin Solid Films* 517: 1457-60

Babu, G. S., Y.B. K. Kumar, P. U. Bhaskar, S. R. Vanjari. 2010. " Effect of Cu/(Zn+Sn) ratio on the properties of co-evaporated $Cu_2ZnSnSe_4$ thin films", *Solar Energy Materials and Solar Cells*, 94: 221-26

Batchelor, W K, I L Repins, J Schaefer, and M E Beck. 2004. "Impact of Substrate Roughness on $CuIn_XGa_{1-X}Se_2$ Device Properties", *Solar Energy Materials and Solar Cells* 83(1): 67–80.

Blösch, Patrick, A. Chirila , F. Pianezzi, S. Seyrling, P. Rossbach, ˇS. Buecheler, S. Nishiwaki, A. N. Tiwari, "Comparative Study of Different Back-Contact Designs for High-Efficiency CIGS Solar Cells on Stainless Steel Foils", *IEEE Journal of Photovoltaics* 1(2)*:*194-99

Chen, C. Julian. 2011. *Physics of Solar Energy*. Hoboken, NJ, USA: John Wiley & Sons, Inc.

Chen, Shiyou, J-H.Yang, X. G. Gong, A. Walsh, S-H Wei. 2010. "Intrinsic Point Defects and Complexes in the Quaternary Kesterite Semiconductor Cu_2ZnSnS_4." *Physical Review B* 81 (24): 245204.

Cheng, A-J., M. Manno, A. Khare, C. Leighton, S. A. Campbell, E. S. Aydil. 2011. "Imaging and Phase Identification of Cu_2ZnSnS_4 Thin Films Using Confocal Raman Spectroscopy." *Journal of Vacuum Science & Technology A: Vacuum, Surfaces, and Films* 29 (5): 051203.

Dai, Pengcheng, G.Zhang, Y. Chen, H. Jiang, Z. Feng, Z.Lin, J. Zhan. 2012a. "Porous Copper Zinc Tin Sulfide Thin Film as Photocathode for Double Junction Photoelectrochemical Solar Cells." *Chemical Communications*, 48 (24): 3006–8.

Edler, Michael, T.Rath, A. Schenk, A. Fischereder, W. Haas, M. Edler, B. Chernev. 2012. "Copper Zinc Tin Sulfide Layers Prepared from Solution Processable Metal Dithiocarbamate Precursors", *Materials Chemistry and Physics*, 136: 582–88.

Ennaoui, A., M. Lux-Steiner, A. Weber, D. Abou-Ras, I. Kötschau, H.-W. Schock, R. Schurr, 2009. "Cu2ZnSnS4 Thin Film Solar Cells from Electroplated Precursors: Novel Low-Cost Perspective." *Thin Solid Films* 517 (7):2511–14.

Ericson, Tove, Tomas Kubart, Jonathan J. Scragg, and Charlotte Platzer-Björkman. 2012. “Reactive Sputtering of Precursors for Cu2ZnSnS4 Thin Film Solar Cells.” *Thin Solid Films* 520 (24):7093–99.

Farinella, M, R.Inguanta, T. Spanò, P. Livreri, S. Piazza, C. Sunseri. 2014. “Electrochemical Deposition of CZTS Thin Films on Flexible Substrate.” *Energy Procedia* 44:105–10.

Fernandes, P. A, P. M. P Salomé, A. F. Cunha. 2011. “Study of Polycrystalline Cu2 ZnSnS4 Films by Raman Scattering.” *Journal of Alloys and Compounds* 509 (28): 7600–7606.

Fernandes, P A, P M P Salomé, F D. Cunha. 2010. “A Study of Ternary Cu2SnS3 and Cu3SnS4 Thin Films Prepared by Sulfurizing Stacked Metal Precursors.” *Journal of Physics D: Applied Physics* 43 (21): 215403.

Flammersberger, Hendrik. 2010. “Experimental Study of Cu2ZnSnS4 Thin Films for Solar Cells”, M.Sc. Thesis, Uppsala University.

Friedlmeier, T. M., N. Wieser, T.Walter, H. Dittrich, H. W. Schock. 1997. "Heterojunctions based on Cu2ZnSnS4 and Cu2ZnSnSe4 thin films" 14th European PSVEC and Exhibit., P4B.10

Gemelli, E., N.H.A. Camargo, "Oxidation Kinetics of Commercially Pure Titanium" *Revista Materia*, 12 (2007) 525-531

Hartmann, M, M Schmidt, A Jasenek, and H W Schock. F. Kessler, K.Herz, M. Powalla, 2000.“Flexible and light weight substrates for Cu(In,Ga)Se2 solar cells and modules" , 28th IEEE PVSC, Anchorage, USA, 638-41

Heavens, O. S., 1970. Thin Film Physics, Methuen and Co,Ltd. London,

Hiroi, Homare, N. Sakai, T.Kato, H. Sugimoto, S. Shell K K. Sekiyu 2013. “High Voltage Cu2ZnSnS4 Submodules by Hybrid Buffer Layer”,IEEE Photovoltaic Specialist Conference 39th Tampa, 863–66.

Ito, K., Nakazawa T.1988. "Electrical and Optical Properties of Stannite-Type Quaternary Semiconductor Thin Films", *Jpn. J. Appl*. Phys. 27: 2094-97

Jackson, Philip, D. Hariskos, R. Wuerz, W. Wischmann, M.Powalla. 2014. “Compositional investigation of potassium doped Cu(In,Ga)Se2 solar cells with efficiencies up to 20.8%”, *Pyhsica Status Solidi (RRL) Rapid Research Letters* 8(3):219-22

Jiang, Minlin. 2011. “Cu_2ZnSnS_4 Polycrystalline Thin Films with Large Densely Packed Grains Prepared by Sol-Gel Method.” *Journal of Photonics for Energy* 1 (1):019501-1

Jimbo, Kazuo, R. Kimura, T. Kamimura, S. Yamada, W. S. Maw, H. Araki, K. Oishi, H. Katagiri. 2007. “Cu_2ZnSnS_4-Type Thin Film Solar Cells Using Abundant Materials.” *Thin Solid Films* 515 (15): 5997–99.

Jones, Geoffrey., L. Bouamane. 2012. "' Power from Sunshine ': A Business History of Solar Energy ' Power from Sunshine ': A Business History of Solar Energy.", Working Paper, Harvard Business School, 12:105

Katagiri, Hironori, N. Sasaguchi, S. Hando, S. Hoshino, J. Ohashi, T.Yokota. 1997. "Preparation and Evaluation of Cu_2ZnSnS_4 Thin Films by Sulfurization of E-B Evaporated Precursors." *Solar Energy Materials and Solar Cells* 49 (1-4): 407–14.

Katagiri, Hironori, K. Jimbo, W. S. Maw, K. Oishi, M. Yamazaki, H. Araki, A. Takeuchi. 2009. "Development of CZTS-Based Thin Film Solar Cells." *Thin Solid Films* 517 (7): 2455–60.

Kessler, Friedrich, Dominik Rudmann. 2004. "Technological Aspects of Flexible CIGS Solar Cells and Modules", *Solar Energy*, 77(6): 685–95.

Krishnamurti, D.1962. The Raman Spectrum of Rutile, *Proceedings of the Indian Academy of Sciences - Section A*, 55(5): 290-9

Lin, Xianzhong, J. Kavalakkatt, K.Kornhuber, S. Levcenko, M. C. Lux-Steiner, A. Ennaoui. 2012. "Structural and Optical Properties of Cu2ZnSnS4 Thin Film Absorbers from ZnS and Cu_3SnS_4 Nanoparticle Precursors.", *Thin Solid Films,* 535:10-13

Liu, Fangyang, Y. Li, K. Zhang, B. Wang, C. Yan, Y. Lai, Z. Zhang, J. Li, Y. Liu. 2010. "In Situ Growth of Cu_2ZnSnS_4 Thin Films by Reactive Magnetron Co-Sputtering." *Solar Energy Materials and Solar Cells* 94 (12): 2431–34.

Maeda, T, T Takeichi, T Wada. 2006. "Systematic Studies on Electronic Structures of $CuInSe_2$ and the Other Chalcopyrite Related Compounds by First Principles Calculations." *Physica Status Solidi (a)* 203(11): 2634–38.

Maeda, Kazuya, K. Tanaka, Y. Fukui, H.Uchiki. 2011. "Influence of H2S Concentration on the Properties of Cu_2ZnSnS_4 Thin Films and Solar Cells Prepared by Sol–gel Sulfurization." *Solar Energy Materials and Solar Cells* 95 (10): 2855–60.

Mali, Sawanta S., B. M. Patil, C. A. Betty, P. N. Bhosale, Y.W. Oh, S. R. Jadkar, R. S. Devan, Y.-R. Ma, P. S. Patil. 2012. "Novel Synthesis of Kesterite Cu_2ZnSnS_4 Nanoflakes by Successive Ionic Layer Adsorption and Reaction Technique: Characterization and Application." *Electrochimica Acta* 66: 216–21.

Mitzi, David B, O.Gunawan, T. K Todorov, K.Wang, S. Guha. 2011a. "The Path towards a High-Performance Solution-Processed Kesterite Solar Cell", *Solar Energy Materials & Solar Cells*, 95: 1421–36.

Mitzi, David B., O. Gunawan, T.K. Todorov, K. Wang, S. Guha. 2011b. "The Path towards a High-Performance Solution-Processed Kesterite Solar Cell." *Solar Energy Materials and Solar Cells* 95:1421–36.

Moholkar, A V, S S Shinde, A R Babar, Kyu-ung Sim, Ye-bin Kwon. 2011. "Development of CZTS Thin Films Solar Cells by Pulsed Laser Deposition : Influence of Pulse Repetition Rate." *Solar Energy* 85 (7): 1354–63.

Olekseyuk, I D, I V Dudchak, L V Piskach. 2004. "Phase Equilibria in the Cu_2S-ZnS-SnS_2 System", *J. Alloys Compounds* 368: 135–43.

Olson, S., 2011."NREL confirms world-record 43.5% efficiency on Solar Junction's CPVcell"14 April 2011, http://www.pvtech.org/news/nrel_confirms_world_record_43.5_efficiency_on_solar_junctions_cpv_cell

Paier, Joachim, R. Asahi, A. Nagoya, G. Kresse. 2009. "Cu2ZnSnS4 as a Potential Photovoltaic Material : A Hybrid Hartree-Fock Density Functional Theory Study.", *Phys. Rev. B* 79(11):115126

Patel, M, I Mukhopadhyay, A. Ray. 2012. "Structural, Optical and Electrical Properties of Spray-Deposited CZTS Thin Films under a Non-Equilibrium Growth Condition." *Journal of Physics D: Applied Physics* 45 (44): 445103.

Parenteau, M., Carlone C., "Influence of temperature and pressure on electronic transions in SnS and SnSe semiconductors." *Phys. Rev. B.* 41(8):5227-34

Pouilleau, J., D. Devilliers, F. Garrido, S. Durand-Vidal, E. Mahe, 1997. "Structure and Composition of Passive Titanium Oxide Films" *Materials Science and Engineering, v*. B47: 235-243

Rajeshmon, V.G., C. S. Kartha, K.P. Vijayakumar, C. Sanjeeviraja, T. Abe, Y. Kashiwaba. 2011. "Role of Precursor Solution in Controlling the Opto-Electronic Properties of Spray Pyrolysed Cu_2ZnSnS_4 Thin Films." *Solar Energy* 85 (2).

Razykov, T M, C S Ferekides, D Morel, E Stefanakos, and H S Ullal. 2011. "Solar Photovoltaic Electricity : Current Status and Future Prospects." *Solar Energy* 85 (8). 1580–1608.

Reinhard, Patrick, A. Chiril, B. Patrick, F. Pianezzi, S. Nishiwaki, S. Buecheler, A. N Tiwari. 2013. "Review of Progress Toward 20 % Efficiency Flexible CIGS Solar Cells and Manufacturing Issues of Solar Modules" IEEE Journal of Photovoltaics, 3 (1): 572–80.

Sandoval, S. J., D. Yang, R.F. Frindt, J.C. Irwin, 1991."Raman study and lattice dynamics of single molecular layers of MoS_2", *Phys. Rev. B. Condens Matter*. 44(8):3955-62

Schorr, S. 2007. "Structural Aspects of Adamantine like Multinary Chalcogenides." *Thin Solid Films*, 515 (15): 5985–91.

Schubert, B-A., Cinque, Sonja, T. Unold, R. Klenk, S. Schorr, H.-W. Schock. 2011. "Cu_2ZnSnS_4 Thin Film Solar Cells by Fast Coevaporation", P*rogress in Photovoltaics: Research and Applications*, 19(1): 93–96.

Scragg, Jonathan J, P. J Dale, L. M Peter. 2008. “Towards Sustainable Materials for Solar Energy Conversion : Preparation and Photoelectrochemical Characterization of Cu_2ZnSnS_4”, *Electrochemistry Communications*, 10(4): 639–42.

Scragg, Jonathan James. 2010. “Studies of Cu_2ZnSnS_4 Films Prepared by Sulfurisation of Electrodeposited Precursors.” Doctor of Philosophy (PhD)Thesis, University of Bath

Scragg Jonathan James., J. T. Watjen, M. Efoff, T. Ericson, T. Kubart, C. Platzer-Björkman. 2012. "A detrimental reaction at the molybdenum back contact in $Cu_2ZnSn(S,Se)_4$ thin-film solar cells", *J. Am. Chem. Soc*., 134 19330-19333

Scragg, Jonathan James, T. Kubart, J T. Wa, T. Ericson, M. K. Linnarsson, and Charlotte Platzer-Björkmann. 2013. “Effects of Back Contact Instability on Cu_2ZnSnS_4 Devices and Processes", *Chem. Mater*. 25: 162-3171

Shockley, W., H. J. Queisser, 1961. "Detailed Balance Limit of Efficiency of p-n Junction Solar Cells." *J. Appl. Phys.* 32: 510-19

Takeuchi, M., Y. Abe, Y. Yoshida, Y. Nakayama, M. Okazaki, and Y. Akagawa. 2003. “Acid Pretreatment of Titanium Implants.” *Biomaterials* 24 (10): 1821–27.

Tanaka, Kunihiko, Y. Fukui, N. Moritake, H. Uchiki. 2011. “Chemical Composition Dependence of Morphological and Optical Properties of Cu_2ZnSnS_4 Thin Films Deposited by Sol–gel Sulfurization and Cu_2ZnSnS_4 Thin Film Solar Cell Efficiency.” *Solar Energy Materials and Solar Cells* 95 (3):838–42.

Tanaka, Kunihiko, M. Kato, H. Uchiki. 2014. “Effects of Chlorine and Carbon on Cu2ZnSnS4 Thin Film Solar Cells Prepared by Spray Pyrolysis Deposition.” *Journal of Alloys and Compounds*,

Tanaka, Tooru, D. Kawasaki, M. Nishio, Q.Guo, H. Ogawa. 2006. “Fabrication of Cu_2ZnSnS_4 Thin Films by Co-Evaporation.” *Physica Status Solidi C*., 8: 2844–47.

Tanusevski A., D. Poelman. 2003. "Optical and photoconductive properties of SnSthin films prepared by electron beam evaporation", *Sol. Energy Mater. Sol. Cells* 80 : 297–303.

Wagner, S., H. Gleskova, I-C. Cheng, M. Wu, 2003. "Silicon for thin-film transistors" *Thin Solid Films* 430:15-19.

Walker, Perrin, and William H Tarn. 1991. Handbook of Metal Etchants,CRC.

Wang, W., M.T. Winkler, O. Gunawan, T. Gokmen, T.K. Todorov, Y. Zhu, D.B. Mitzi, "Device Characteristics of CZTSSe Thin-Film Solar Cells with 12.6% Efficiency." *Advanced Energy Materials* 4(7) (2013)

Weaire, D.1975.“The Structure of Chalcopyrite Semiconductors”, Journal De Physique, 9:27-29.

Wiemer, M., V. Sabnis, and H. Yuen, “43.5% efficient lattice matched solar cells in High and Low Concentrator Systems for Solar Electric Applications" 810804 of Proceedings of SPIE, San Diego, Calif, USA, September 2011

Winkler, M., J. Griesche, I. Konovalov, J. Penndorf, J. Wienke, and O. Tober. 2004. “CISCuT—solar Cells and Modules on the Basis of CuInS2 on Cu-Tape.” *Solar Energy* 77 (6): 705–16.

Yagioka, Takeshi, T. Nakada. 2009. “Cd-Free Flexible Cu(In,Ga)Se 2 Thin Film Solar Cells with ZnS(O,OH) Buffer Layers on Ti Foils.” *Applied Physics Express* 2: 072201.

Yang, Kee-jeong, J.-H Sim, B. Jeon, D-H Son, D-H Kim, S-Joon Sung, D-K Hwang. 2014. “Effects of Na and MoS2 on Cu2ZnSnS4 Thin Film Solar Cell.” *Prog. Photovolt: Res. Appl.* DOI: 10.1002/pip.2500.

Yoo, Hyesun, J. Kim. 2011. “Comparative Study of Cu2ZnSnS4 Film Growth.” *Solar Energy Materials & Solar Cells* 95: 239–44.

Zhou, Zhihua, Y. Wang, D. Xu, Y.Zhang. 2010a. "Fabrication of Cu2ZnSnS4 Screen Printed Layers for Solar Cells.” *Solar Energy Materials and Solar Cells* 94 (12):2042–45.